

Effects of Electrochemical Conditioning on Nickel-Based Oxygen Evolution Electrocatalysts

Yoon Jun Son, Seonwoo Kim, Vanessa Leung, Kenta Kawashima, Jungchul Noh, Kihoon Kim, Raul A. Marquez, Omar A. Carrasco-Jaim, Lettie A. Smith, Hugo Celio, Delia J. Milliron, Brian A. Korgel, and C. Buddie Mullins*



Cite This: *ACS Catal.* 2022, 12, 10384–10399



Read Online

ACCESS |

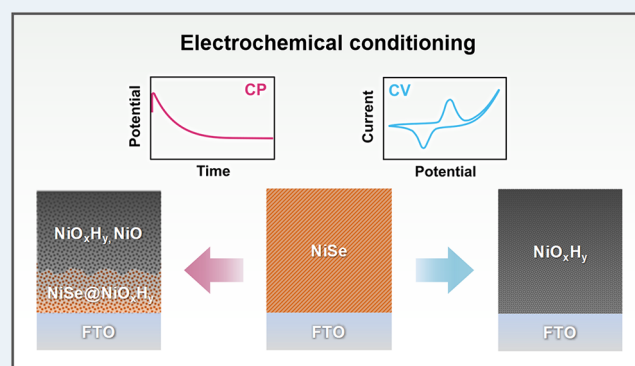
Metrics & More

Article Recommendations

Supporting Information

ABSTRACT: Electrochemical conditioning *via* chronopotentiometry (CP) and cyclic voltammetry (CV) is essential for the activation of oxygen evolution reaction (OER) electrocatalysts. While many reports have activated OER electrocatalysts using either CP or CV, the inherent differences between these two electrochemical conditioning methods for the activation of OER electrocatalytic materials have yet to be explored. Here, we investigate the effects of CP and CV electrochemical conditioning on a Ni-based OER precatalyst and substrate in Fe-purified and Fe-unpurified KOH electrolytes by employing (i) Ni foil, (ii) NiSe precatalyst films with different thicknesses on the fluorine-doped tin oxide glass substrate, and (iii) NiSe precatalyst films on Ni foil substrates. It was found that CV electrochemical conditioning can result in a higher degree of *in situ* oxidation and Fe incorporation for Ni-based precatalysts and substrates compared to CP electrochemical conditioning. In turn, this brought about different material properties (*e.g.*, *in situ* oxidized layer thickness, composition, crystallinity, and morphology) and electrochemical characteristics (*e.g.*, active surface area, electron transport limitation, and intrinsic activity) of Ni-based electrocatalysts, thereby not only affecting their OER activity but also complicating the interpretation of the origin of OER activity. This study identifies the distinct effects of CP and CV electrochemical conditioning on Ni-based OER electrocatalysts and provides insight into the choice of the electrochemical conditioning method to better investigate OER electrocatalysts.

KEYWORDS: oxygen evolution reaction, electrocatalyst, water splitting, electrochemical conditioning, electrochemical activation, chronopotentiometry, cyclic voltammetry



1. INTRODUCTION

For efficient electrochemical water splitting, it is crucial to improve the sluggish kinetics of the oxygen evolution reaction (OER). While noble metal-based oxides (*e.g.*, IrO_x and RuO_x) are benchmark electrocatalysts for the OER in acidic electrolytes, their high cost and scarcity have spurred the search for inexpensive and earth-abundant electrocatalysts.^{1,2} In this regard, 3d-transition metal (*e.g.*, Ni, Co, and Fe)-based compound materials (*e.g.*, borides, carbides, pnictides, and chalcogenides) have gained attention in recent years owing to their low cost, earth abundance, and high OER activity under alkaline conditions.^{3–6} Due to their thermodynamic instability under OER conditions, however, most transition metal compounds act as precatalysts and undergo *in situ* oxidation. This *in situ* oxidation results in compositional transformation to metal hydr(oxy)oxides (MO_xH_y) that act as real OER active species as well as structural reorganization to nanoporous structures with increased surface area, which can significantly affect the OER activity and stability.^{3,7,8} Also, depending on

the specific electrocatalytic material, different degrees of *in situ* oxidation can occur: either (i) complete *in situ* oxidation wherein the entire transition metal compound is completely oxidized or (ii) partial *in situ* oxidation wherein the surface of the transition metal compound is converted to MO_xH_y, while the underlying transition metal compound remains unoxidized, forming a core–shell structure (transition-metal compound core–MO_xH_y shell) or a composite of transition metal compound and MO_xH_y.^{3,6,7}

Among promising transition metal-based OER electrocatalysts, NiFe-based catalysts have shown the best OER

Received: February 25, 2022

Revised: July 13, 2022

Published: August 9, 2022



activity in alkaline electrolytes.^{9–12} The optimal composition of NiFe-based catalysts that show the highest OER performance lies in the range of 10–25% Fe.^{13,14} NiFe-based catalysts have been prepared *via* a multitude of methods, and recently, it has been found that they can be prepared *via in situ* incorporation of Fe ions into NiO_xH_y during the OER. Trotochaud *et al.* studied the OER of Ni(OH)₂ in Fe-purified and Fe-unpurified KOH electrolytes and showed that even sub-ppm levels of Fe in the Fe-unpurified KOH electrolyte are readily incorporated into Ni(OH)₂, forming NiFeOOH throughout the electrolyte-permeable structure of Ni(OH)₂.¹¹ Friebel *et al.* found that Ni(OH)₂ film can absorb Fe up to a solubility limit of ~25% Fe.¹³ These previous studies indicate that it is possible to prepare highly efficient NiFe-based catalysts by using *in situ* Fe incorporation into Ni-based materials during the OER in Fe-unpurified KOH electrolytes.

Electrochemical conditioning employing chronopotentiometry (CP), chronoamperometry (CA), and cyclic voltammetry (CV) is essential for the activation of OER electrocatalysts before activity measurement as well as for long-term stability testing. So far, different electrochemical conditioning methods (*e.g.*, CP, CA, and CV) have been employed without clear distinction for various OER electrocatalysts and random electrochemical activation results (*e.g.*, degree of *in situ* oxidation and Fe incorporation) have been reported.^{10,15–24} Kim *et al.* conducted CV electrochemical conditioning for Co₃C and observed its complete *in situ* oxidation to amorphous CoO_x.²² Kawashima *et al.* conducted CV electrochemical conditioning for Ni₃N/Ni foam in Fe-purified and Fe-unpurified KOH electrolytes and observed its partial *in situ* oxidation and Fe incorporation into Ni₃N/Ni.²³ In comparison, Trotochaud *et al.* carried out CP electrochemical conditioning for NiO and observed its complete *in situ* oxidation to NiO_xH_y in alkaline media (1 M KOH).¹⁰ Clament Sagaya Selvam *et al.* conducted CA electrochemical conditioning for Ni(OH)₂/Co₉S₈ in 1 M KOH electrolyte containing 1 ppm of Fe ions and observed its complete *in situ* oxidation and Fe incorporation to form Fe-doped NiOOH/CoOOH.¹⁷ Menezes *et al.* performed CA electrochemical conditioning in 1 M KOH and observed partial *in situ* oxidation of Ni₁₂P₅ and Ni₂P, forming a nickel phosphide core and amorphous Ni(OH)₂/NiOOH shell.²⁴ May *et al.* conducted both CV and CA electrochemical conditioning for various Ba-, Sr-, Co-, and Fe-based perovskite oxides in 0.1 M KOH and reported their different degree of amorphization depending on the surface atomic structure and chemistry of oxides.²⁵ Schäfer *et al.* and Moureaux *et al.* conducted electrochemical conditioning (*e.g.*, CP, CV, and alternating potential steps) for stainless steels and created NiFe-based oxides with different material properties.^{26,27}

In the aforementioned studies, considering that electrocatalysts with various material properties (*e.g.*, composition, crystallinity, grain size, thickness of catalyst layer, and porous morphology) were studied, the observed electrochemical activation results would be correlated to their distinct material properties. However, given the difference between electrochemical conditioning methods such that CP (or CA) involves the application of only anodic OER potential while CV has repetitive cathodic potential sweeps alternating with anodic potential sweeps, the choice of electrochemical conditioning method may also influence the observed electrochemical activation results (*e.g.*, degree of *in situ* oxidation and Fe incorporation) and OER activity. However, due to distinct

material properties of various OER electrocatalysts and random usage of electrochemical conditioning methods in the previous studies, the effects of different electrochemical conditioning methods on the degree of *in situ* oxidation and Fe incorporation of OER electrocatalysts are difficult to deduce and thus remain elusive. In this regard, a controlled study that performs electrochemical conditioning of OER electrocatalysts with the same material properties is necessary to identify the effects of CP (or CA) and CV electrochemical conditioning on the electrochemical activation processes and OER activity. In addition, Ni-based substrates, such as Ni foam and Ni foil, have been widely used as substrates for OER electrocatalysts due to their high electrical conductivity and robustness.^{28–32} However, considering that electrochemically activated OER electrocatalysts have electrolyte-permeable structures and Ni is an OER active material,^{11,33} there is a possibility that Ni-based substrates may also be exposed to the electrolyte, undergo *in situ* oxidation during electrochemical conditioning, and be involved in the OER, which requires further investigation.

Herein, we aim to identify the effects of CP and CV electrochemical conditioning on a Ni-based OER precatalyst and substrate in Fe-purified and Fe-unpurified KOH electrolytes. To evaluate these effects, we conducted CP and CV electrochemical conditioning for three different sets of controlled samples: (i) Ni metal foil to understand the fundamental characteristics of CP and CV electrochemical conditioning, (ii) NiSe films with different thicknesses (or loadings) on fluorine-doped tin oxide glass (FTO) substrate to solely examine the influence of different electrochemical conditioning methods on Ni-based compound precatalysts, and (iii) NiSe films on Ni foil substrates to investigate how Ni-based substrates can be involved in the observed OER characteristics and activity, which are summarized in Table S1. By performing electrochemical analyses and material characterizations before and after the OER, we demonstrated that CV electrochemical conditioning can bring about a higher degree of *in situ* oxidation and Fe incorporation for OER precatalysts and Ni-based substrates compared to CP electrochemical conditioning. This results in distinct material properties (*e.g.*, *in situ* oxidized thickness, composition, crystallinity, and morphology), electrochemical characteristics (*e.g.*, active surface area, electron transport limitation, and intrinsic activity), and OER behavior. Based on these findings, we provide insight into the proper choice of the electrochemical conditioning method to efficiently and accurately investigate the OER electrocatalysts.

2. RESULTS AND DISCUSSION

2.1. Understanding CP and CV Characteristics Using Ni Foil.

Given that Ni is one of the most commonly used OER active transition metals in the alkaline electrolyte and substrate material (*e.g.*, Ni foam and Ni foil) for OER electrocatalysts,^{28–32} Ni foil is a suitable choice for the study of the fundamental characteristics of CP and CV electrochemical conditioning methods for alkaline OER electrocatalysts. Although electrochemical behaviors of Ni in alkaline media have been widely studied,^{34–37} it needs further investigation focused on material properties and OER characteristics of Ni after CP and CV electrochemical conditioning in both Fe-purified and Fe-unpurified alkaline electrolytes. In this regard, the effects of CP and CV electrochemical conditioning on Ni foil were investigated in Fe-purified and Fe-unpurified 1 M KOH electrolytes. Here, the Fe composition of each electrolyte

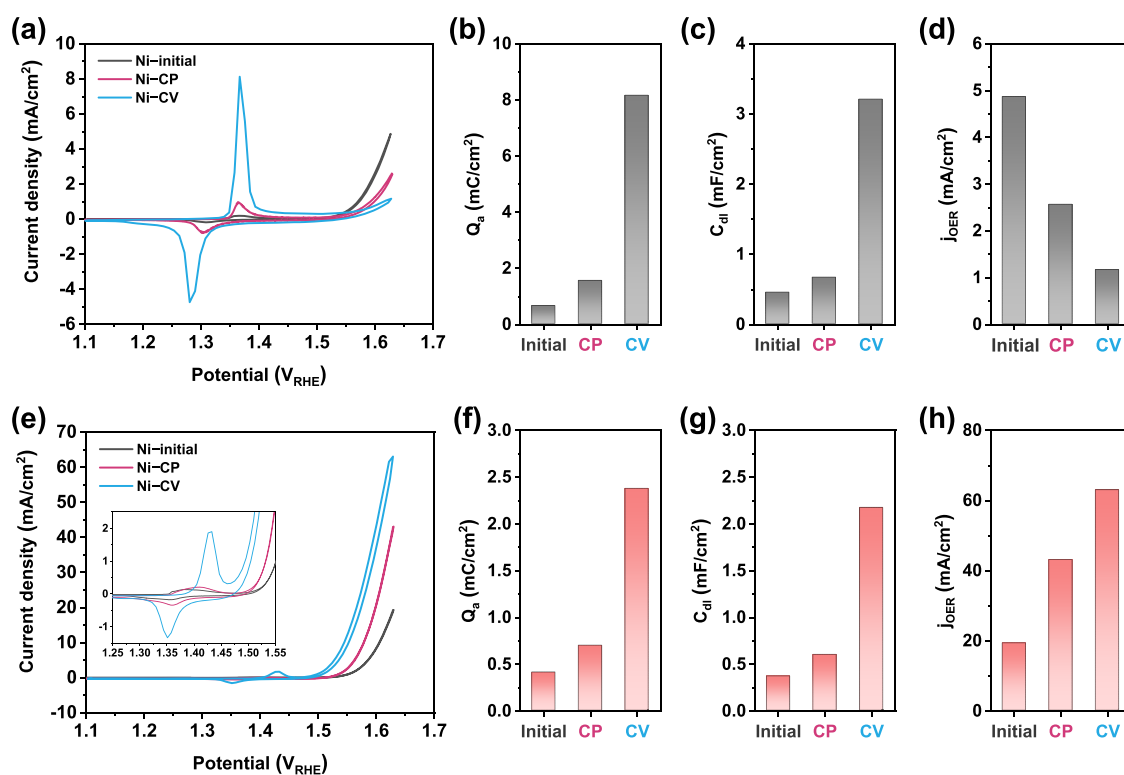


Figure 1. Electrochemical analyses of Ni foil before and after CP and CV electrochemical conditioning in (a–d) Fe-purified and (e–h) Fe-unpurified 1 M KOH electrolytes. (a) CV curves at a scan rate of 20 mV/s, (b) Q_a , (c) C_{dl} from EIS at 1.63 V_{RHE} , and (d) j_{OER} at 1.63 V_{RHE} . (e) CV curves at a scan rate of 20 mV/s (inset shows the magnified $Ni^{2+/3+}$ redox peaks), (f) Q_a , (g) C_{dl} from EIS at 1.63 V_{RHE} , and (h) j_{OER} at 1.63 V_{RHE} .

was examined using ICP-MS (Table S2). CP and CV electrochemical conditioning of Ni foil were conducted at 5 mA/cm² under OER potentials for 24 h and in the potential range of 1.1 to 1.63 V vs the reversible hydrogen electrode (V_{RHE}) for more than 1000 cycles, respectively, until there was no significant change in the OER activity or redox charge for $Ni^{2+/3+}$ transition in subsequent CV measurements after electrochemical conditioning (Figure S1).

Figure 1a–d shows the electrochemical analysis results of Ni foil before and after electrochemical conditioning in Fe-purified 1 M KOH electrolyte; Ni foil before electrochemical conditioning and after CP and CV electrochemical conditioning were denoted as Ni-initial, Ni-CP, and Ni-CV, respectively. From the CV curves in Figure 1a, the anodic redox peak at around 1.37 V_{RHE} is attributed to the transition of $Ni(OH)_2$ (Ni^{2+}) to $NiOOH$ (Ni^{3+}). The anodic redox charge associated with the Ni^{2+} to Ni^{3+} transition (Q_a), which is related to the number of electrochemically redox-active Ni cations exposed to the electrolyte, was calculated from the CV curves. Figure 1b presents that after CP and CV electrochemical conditioning, Q_a of Ni-CP and Ni-CV increased compared to that of Ni-initial. The reason Q_a increased after electrochemical conditioning is that Ni metal was *in situ* oxidized during the electrochemical conditioning and transformed into hydrous NiO_xH_y , which can join the $Ni^{2+/3+}$ redox reaction as well as act as OER active species.^{15,21,38} The Q_a for Ni-CV was significantly higher than that for Ni-CP, implying that Ni-CV underwent more *in situ* oxidation and created a thicker NiO_xH_y layer compared to Ni-CP. The difference in the degree of *in situ* oxidation between Ni-CP and Ni-CV is attributed to the partial reduction of the NiO_xH_y layer during the cathodic sweeps of CV.^{38–40} To be specific, as for Ni-CP, when Ni

metal is oxidized under anodic potentials, a hydrous oxide layer is formed with a thin and compact anhydrous oxide layer underneath. Further oxidation of Ni metal to a hydrous oxide layer is limited due to the high kinetic barrier for ion migration in the compact oxide layer. As for Ni-CV, however, the cathodic sweep following the anodic sweep can partially reduce the anhydrous oxide layer and facilitate the rearrangement of oxyanion species into a disrupted state. This disrupted oxyanion species not only is more susceptible to further oxidation in the subsequent anodic sweeps but can also be incorporated into the hydrous oxide layer during further cathodic sweeps, which leads to growing a thicker hydrous oxide layer at the expense of the underlying metal.

To obtain the double-layer capacitance (C_{dl}), which can be used to estimate the surface area of electrocatalysts exposed to the electrolyte,⁴¹ electrochemical impedance spectroscopy (EIS) analysis was conducted at 1.63 V_{RHE} . Figure S2a–c displays the Bode and Nyquist plots of the EIS spectra for the Ni-initial, Ni-CP, and Ni-CV samples. From the semicircle of the Nyquist plots at lower frequencies, the C_{dl} values were obtained by fitting the EIS data employing the equivalent circuit in Figure S3a (see the Supporting Information for details related to EIS analysis). As displayed in Figure 1c, the C_{dl} value increased after electrochemical conditioning, and Ni-CV had a higher C_{dl} value than Ni-CP. A similar trend in C_{dl} and Q_a can be explained by the thickness of the hydrous NiO_xH_y layer on Ni foil after electrochemical conditioning and the corresponding surface area of fragments of hydrous NiO_xH_y exposed to the electrolyte.

The OER activity that can be represented by the OER current density normalized by geometric area (j_{OER}) at 1.63 V_{RHE} was compared in Figure 1d, and Ni-initial showed the

highest OER activity followed by Ni-CP and Ni-CV. Considering that Q_a and C_{dl} values are commonly used to represent the electrochemical active surface area of electrocatalysts,^{41,42} it might seem counterintuitive that the trend of j_{OER} was opposite to the trend of Q_a and C_{dl} ; the Ni-CV sample that had the highest Q_a and C_{dl} showed the lowest OER activity. To understand this OER activity trend, it is necessary to investigate the effects of OER performance governing factors, such as intrinsic activity (*i.e.*, the rate of production of O_2 molecules per catalytic active site) and electron and mass transport together with active surface area.^{33,43,44} The specific activity is quite useful in comparing the intrinsic activity of catalysts with the different number of active sites despite its limitations of inaccuracy in measuring the real catalytic active sites and interference of transport limitation.^{9,41,45–48} The specific OER activity for Ni-initial, Ni-CP, and Ni-CV was calculated by normalizing the j_{OER} by Q_a or C_{dl} (Figure S4). Both j_{OER}/Q_a and j_{OER}/C_{dl} decreased significantly in the order of Ni-initial > Ni-CP > Ni-CV. This implies (1) the decrease of intrinsic activity or (2) increase of electron and mass transport limitation in the order of Ni-initial < Ni-CP < Ni-CV. The Tafel slope, which is determined by intrinsic activity and transport properties of the electrocatalyst, was also compared; a lower Tafel slope means higher intrinsic activity and less transport limitation.³³ Tafel slope increased in the order of Ni-initial (65.2 mV dec⁻¹) < Ni-CP (77.3 mV dec⁻¹) < Ni-CV (135 mV dec⁻¹), which aligns with the specific activity trend (Figure S5).

First, intrinsic activity was considered to understand the observed OER activity trend. The different intrinsic activity of Ni-initial, Ni-CP, and Ni-CV can be attributed to their different crystal phases of NiO_xH_y . The electrochemical conditioning of Ni-based materials can not only form amorphous hydrous oxides like other transition metals (*e.g.*, Ru, Ir, *etc.*)^{39,49} but also grow 2D layered structures of NiO_xH_y ^{50,51} which consists of α -Ni(OH)₂, γ -NiOOH, β -Ni(OH)₂, and β -NiOOH. It has been reported that α -Ni(OH)₂/ γ -NiOOH phases can be transformed into β -Ni(OH)₂/ β -NiOOH phases *via* electrochemical conditioning or aging (*i.e.*, loss of water, cations, and anions in the interlayers by immersion in alkaline media)^{39,50} and that the α -Ni(OH)₂/ γ -NiOOH phases have higher intrinsic activity than β -Ni(OH)₂/ β -NiOOH phases in the Fe-purified alkaline electrolyte.^{11,14} Thus, the lower intrinsic activity of Ni-CP and Ni-CV compared to Ni-initial can be due to their greater portion of β -Ni(OH)₂/ β -NiOOH over α -Ni(OH)₂/ γ -NiOOH after electrochemical conditioning. Also, compared to Ni-CV, Ni-CP is expected to have a lower portion of the β -Ni(OH)₂/ β -NiOOH phases over the α -Ni(OH)₂/ γ -NiOOH phases because CP electrochemical conditioning was conducted under the OER potential region exceeding 1.565 V_{RHE}, where overcharging of β -NiOOH to γ -NiOOH occurs.¹⁴ This was confirmed by grazing incidence X-ray diffraction (GIXRD) and Raman spectra results of Ni-CP and Ni-CV that Ni-CV has a mixture of α - and β -Ni(OH)₂, whereas Ni-CP consists of mainly α -Ni(OH)₂ (Figure S6; see the Supporting Information for details related to GIXRD and Raman spectra analyses). Nevertheless, the OER activity trend of Ni-initial, Ni-CP, and Ni-CV is not fully explained by their crystalline phase and resulting intrinsic activity alone. For example, although Ni-CV has a higher portion of β -Ni(OH)₂/ β -NiOOH phases, Ni-CV is expected to have a greater amount of α -Ni(OH)₂/ γ -NiOOH compared to Ni-initial

and Ni-CP given its highest Q_a and C_{dl} values. Thus, an additional explanation for the lower OER activity of Ni-CV is still required.

Next, the contribution of electron and mass transport limitation to the observed OER activity was considered. Given that the redox-active Ni sites are closely related to the OER active sites and both the redox reactions for Ni^{2+/3+} and OER accompany the (de)protonation and electron transfer,^{39,52,53} the transport limitation for the redox-active Ni sites was investigated by performing scan-rate dependent CV analyses to deduce any transport limitation issues for the OER (Figure S7). Here, the redox peak current density and scan rate have a relationship of $j = av^b$, where j is the current density, v is the scan rate, a and b are adjustable parameters, and the b -value can be used to identify whether the kinetics of redox reaction is surface-controlled ($b = 1$) or diffusion-controlled ($b = 0.5$).⁵⁴ Figure S7 shows that the redox reaction of Ni-CP ($b \approx 1$) is surface-controlled whereas that of Ni-CV ($b \approx 0.5$) is diffusion-controlled, which is due to charge transport limitation *via* proton–electron hopping between homogeneously distributed redox sites in the thick, hydrated NiO_xH_y layer^{52,53,55} (see the Supporting Information for detailed explanation). Additionally, the extent to which the potential difference between anodic and cathodic redox peaks increases with increasing the scan rate was greater in Ni-CV than in Ni-CP (Figure S7a,d), which also implies severe charge transport limitation for Ni-CV compared to Ni-CP. As to mass transport, it is unlikely that there occurs mass transport limitation of OH⁻, which is a reactant for both redox reaction and OER given enough amounts of OH⁻ in 1 M KOH with pH 14. However, mass transport limitation for removing the products' O_2 bubbles could occur within the electrolyte-permeable but relatively compact NiO_xH_y layer of Ni-CP and Ni-CV, blocking the OER active sites and restricting their actual participation in the OER.⁵⁶ To sum up, it is concluded that the OER activity trend of Ni-initial, Ni-CP, and Ni-CV that is opposite to their Q_a and C_{dl} trends is due to the decreasing intrinsic activity and increasing transport limitation after CP and CV electrochemical conditioning.

Figure 1e–h shows the electrochemical analysis results of Ni foil before and after electrochemical conditioning in Fe-unpurified 1 M KOH electrolyte. From the CV curves in Figure 1e, the anodic redox peaks for the Ni^{2+/3+} transition of Ni-CP and Ni-CV were positively shifted compared to those of Ni-CP and Ni-CV in Fe-purified electrolyte in Figure 1a. This positive redox peak shift is ascribed to the spontaneous incorporation of Fe impurities from the Fe-unpurified electrolyte into the lattice of the NiO_xH_y layer during electrochemical conditioning.^{11,14,33} In Figure 1f,g, Q_a and C_{dl} values showed a similar trend to those in Fe-purified electrolyte; Q_a and C_{dl} increased after electrochemical conditioning, and Ni-CV had higher Q_a and C_{dl} values than Ni-CP. It is noted that compared to Q_a values in the Fe-purified electrolyte, Q_a values in the Fe-unpurified electrolyte were smaller due to the suppression of the Ni^{2+/3+} redox reaction by Fe ions incorporated into NiO_xH_y .^{33,57,58} The OER activity of Ni foil during electrochemical conditioning was enhanced due to the formation of Fe-doped NiO_xH_y *via* Fe incorporation that has superb intrinsic OER activity compared to pure NiO_xH_y (Figure S1b).^{11,33} Figure 1h shows that the j_{OER} values for Ni-initial, Ni-CP, and Ni-CV in the Fe-unpurified electrolyte were higher than those in the Fe-purified electrolyte. Also, Ni-CV exhibited the highest OER activity in

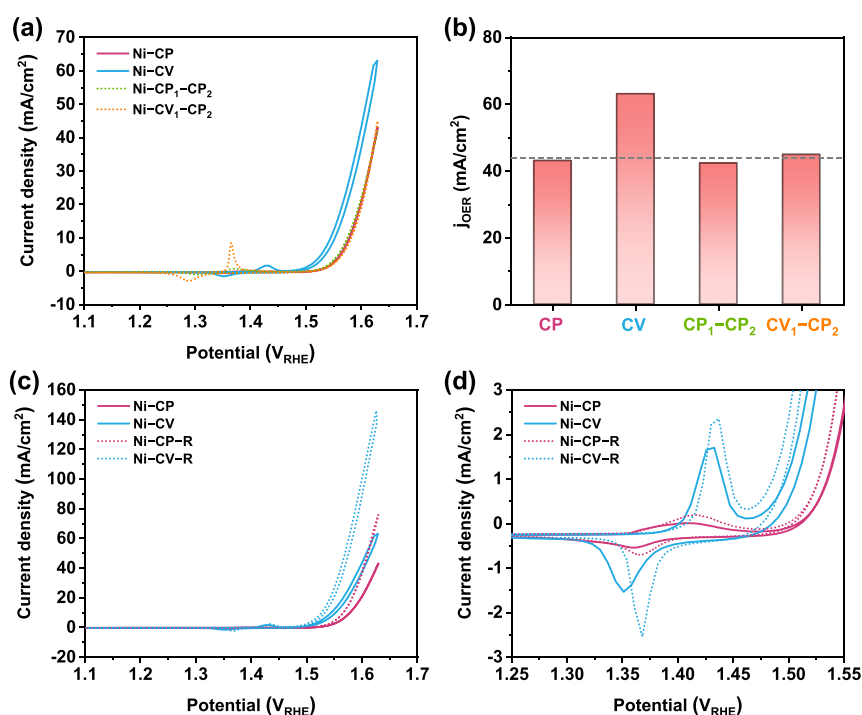


Figure 2. (a) CV curves at a scan rate of 20 mV/s and (b) j_{OER} at 1.63 V_{RHE} for the Ni-CP, Ni-CV, Ni-CP₁-CP₂, and Ni-CV₁-CP₂ samples (CP₁ and CV₁ were conducted in Fe-purified 1 M KOH electrolyte, and CP₂ and CV₂ were conducted in Fe-unpurified 1 M KOH electrolyte). (c) CV curves at a scan rate of 20 mV/s and (d) magnified Ni^{2+/3+} redox peaks for the Ni-CP, Ni-CV, Ni-CP-R, and Ni-CV-R samples in Fe-unpurified 1 M KOH electrolyte (reduction potential treatment for Ni-CP-R and Ni-CV-R was conducted at $-0.076 V_{\text{RHE}}$ for 20 min; CV curves for Ni-CP-R and Ni-CV-R were obtained using the third CV cycle after reduction treatment).

the Fe-unpurified electrolyte followed by Ni-CP and Ni-initial, which is opposite to the OER activity trend in the Fe-purified electrolyte as shown in Figure 1d.

To understand this different OER activity trend in the Fe-unpurified electrolyte, the effects of performance governing factors, such as intrinsic activity, transport limitation, and active surface area, need to be considered. To consider the influence of intrinsic activity and transport limitation on OER activity, the Tafel slope analysis was conducted (Figure S8). At low current densities ($0 < \log [j] < 1$), the Tafel slope was in the order of Ni-CP (46.1 mV dec^{-1}) < Ni-CV (48.5 mV dec^{-1}) < Ni-initial (51.5 mV dec^{-1}). This indicates that Ni-CP has the highest OER kinetics followed by Ni-CV and Ni-initial as a result of their intrinsic activity and transport properties. As the current density increased, the Tafel slope increased due to the increased transport limitation, and the degree of increase in the Tafel slope was steeper in Ni-CV than in Ni-CP, which is attributed to more severe transport limitation through the thicker NiO_xH_y layer of Ni-CV compared to Ni-CP; the Tafel slope at $1 < \log [j] < 1.4$ follows the trend of Ni-CP (70.4 mV dec^{-1}) < Ni-CV (74.0 mV dec^{-1}) < Ni-initial (82.0 mV dec^{-1}), and at $\log [j] > 1.4$, the observed trend follows Ni-CP (98.8 mV dec^{-1}) < Ni-CV (126 mV dec^{-1}).

The OER activity of NiFe-based electrocatalysts significantly changes with Fe composition,^{11,13,14} and there is a possibility that the degree of Fe incorporation into NiO_xH_y layers in Fe-unpurified electrolyte may change depending on the electrochemical conditioning method. In this regard, identifying the Fe composition of Fe-doped NiO_xH_y layers of Ni-CP and Ni-CV is critical to better understand their intrinsic activity and Tafel slope trend. To characterize the Fe composition on the surface and in the bulk layer below the surface, X-ray

photoelectron spectroscopy (XPS) analysis employing a Mg source was conducted before and after Ar⁺ sputtering. The Fe composition was obtained by calculating the ratio of the integrated area of the Ni 2p_{3/2} spectra with that of the Fe 2p_{3/2} spectra. The Fe compositions of Ni-CP and Ni-CV were 5.3 and 13.4% on the surface and 2.7 and 14.5% in the bulk (Figure S9 and Table S3). Considering that the optimum Fe composition of NiFe-based electrocatalysts for showing the highest OER activity lies in the range of 10–25% of Fe,^{13,14} it is expected that Ni-CV has superior intrinsic OER activity to Ni-CP both on the surface and in the bulk.

By combining the XPS and Tafel slope analyses, the OER activity in the Fe-unpurified electrolyte can now be better understood in terms of intrinsic activity, transport limitation, and active surface area. As to the Tafel slope results in Figure S8, the lower Tafel slopes of Ni-CP and Ni-CV compared to Ni-initial are attributed to their higher Fe incorporation during electrochemical conditioning and, hence, higher intrinsic activity. Also, the Tafel slope of Ni-CV, which is supposed to have a lower value than that of Ni-CP according to its higher Fe composition and the resulting intrinsic activity, actually had a higher value than that of Ni-CP. This implies that compared to Ni-CP, transport limitation was more severe for Ni-CV due to its thicker NiO_xH_y layer, which is further supported by its steeper increase in Tafel slope with respect to the current density. However, despite its higher Tafel slope, Ni-CV exhibited higher OER activity than Ni-CP. This indicates that the larger active surface area of Ni-CV played a role in making its OER activity higher than that of Ni-CP. In the same way, the lowest OER activity of Ni-initial can be explained by its lowest intrinsic activity and active surface area.

It is noted that the large active surface area of Ni-CV did not lead to the enhancement of OER activity in the Fe-purified electrolyte, and thus, opposite OER activity trends were observed in the Fe-purified and Fe-unpurified electrolytes. This can be understood by examining the role of the thick NiO_xH_y layer in the bulk, which accompanies increased active surface area and transport limitation, in determining the OER activity. In the Fe-unpurified electrolyte, the contribution of increased active surface area to the OER activity (= active surface area \times intrinsic activity) outweighs the loss of OER activity by transport limitation due to the high intrinsic activity of Fe-doped NiO_xH_y , and vice versa in the Fe-purified electrolyte due to the low intrinsic activity of NiO_xH_y . Some might point out that the improved conductivity *via* Fe-doping into NiO_xH_y can relieve the transport limitation.⁵⁷ Nevertheless, severe transport limitation was still observed for Ni-CV with higher Fe compositions. Thus, it is concluded that the different intrinsic activity is mainly responsible for different impacts of active surface area, resulting in the opposite OER activity trends in Fe-purified and Fe-unpurified electrolytes.

Considering that *in situ* Fe incorporation can effectively tailor the OER kinetics of NiO_xH_y as described above, it is critical to clarify the origin of distinct Fe incorporation characteristics depending on the electrochemical conditioning method. First, it was hypothesized that the difference in Fe incorporation between CP and CV may be related to the different material properties of *in situ* formed NiO_xH_y in Ni-CP and Ni-CV. To test this hypothesis, it is necessary to grow a NiO_xH_y layer *in situ* on Ni foil using CP and CV before Fe incorporation. For this, two control samples were prepared *via* a two-step process, wherein Ni foil was electrochemically conditioned using CP or CV in the Fe-purified electrolyte in the first step to grow a NiO_xH_y layer *in situ* on the Ni foil followed by CP in the Fe-unpurified electrolyte in the second step to incorporate Fe into the *in situ* formed NiO_xH_y layer. These two control samples were denoted as Ni-CP₁-CP₂ and Ni-CV₁-CP₂, respectively, wherein the second and third terms correspond to the electrochemical conditioning method used in the first and second steps, respectively.

Figure 2a presents the CV curves of Ni-CP and Ni-CV in Fe-unpurified electrolyte, Ni-CP₁-CP₂, and Ni-CV₁-CP₂. The anodic redox peak potential for $\text{Ni}^{2+/3+}$ transition of Ni-CP, Ni-CP₁-CP₂, and Ni-CV₁-CP₂ was around 1.38 V_{RHE} , which is similar to those of Ni-CP and Ni-CV in Fe-purified electrolyte in Figure 1a. On the other hand, the anodic redox peak potential of Ni-CV was positively shifted considerably with respect to 1.38 V_{RHE} . Given that the shift of anodic redox peak potential is largely affected by Fe composition in the bulk layer of NiO_xH_y rather than that on the surface,^{57,59,60} this implies that (1) Fe incorporation through the bulk layer of NiO_xH_y hardly occurred during the CP not only for Ni-CP and Ni-CP₁-CP₂ but even for Ni-CV₁-CP₂ despite the presence of a thick NiO_xH_y layer created during the CV. Also, the almost identical j_{OER} of Ni-CP, Ni-CP₁-CP₂, and Ni-CV₁-CP₂ in Figure 2b implies that (2) the degree of Fe incorporation on the surface of Ni-CP, Ni-CP₁-CP₂, and Ni-CV₁-CP₂ was almost identical regardless of the presence of a thick NiO_xH_y layer created by CV for Ni-CV₁-CP₂. These speculations about Fe incorporation based on electrochemical analyses were confirmed by XPS analyses (Figures S9 and S10 and Table S3). The surface Fe composition of Ni-CV₁-CP₂ (3.3%) was similar to those of Ni-CP (5.3%) and Ni-CP₁-CP₂ (5.6%) but significantly lower than that of Ni-CV (13.4%). The bulk Fe composition of Ni-

CV₁-CP₂ (2.1%) was similar to those of Ni-CP (2.7%) and Ni-CP₁-CP₂ (2.9%) but significantly lower than that of Ni-CV (13.4%). Additionally, the Fe composition of Ni-CV₁-CP₂ after further Ar^+ sputtering even decreased to 1.4%. These electrochemical and XPS analysis results demonstrate that Fe incorporation *via* CP is not only less facile than *via* CV but also occurs mainly on the surface of the NiO_xH_y layer regardless of the presence of a thick hydrous NiO_xH_y layer before Fe incorporation; additionally, the different degree of Fe incorporation is hardly related to the CP and CV electrochemical conditioning-derived NiO_xH_y properties.

Next, it was hypothesized that the higher degree of Fe incorporation for CV on the surface and in the bulk of NiO_xH_y layer compared to CP may be related to its cathodic sweep across reductive potentials that are more negative with respect to the $\text{Ni}^{2+/3+}$ redox peak potential. To test this hypothesis, two control samples were prepared *via* a two-step process: CP or CV electrochemical conditioning of Ni foil in Fe-unpurified electrolyte followed by a reduction potential treatment at $-0.076 V_{\text{RHE}}$ for 20 min in Fe-unpurified electrolyte. The resulting samples were denoted as Ni-CP-R and Ni-CV-R. As shown in Figure 2c, the OER activity of Ni-CP-R and Ni-CV-R enhanced compared to Ni-CP and Ni-CV, respectively. From the magnified CV curves in Figure 2d, it was observed that the redox peaks for both Ni-CP-R and Ni-CV-R were noticeably shifted toward a more positive potential compared to those of Ni-CP and Ni-CV, implying considerable Fe incorporation into the NiO_xH_y layer during the reduction potential treatment. This result substantiates that the higher degree of Fe incorporation for Ni-CV compared to Ni-CP is associated with the cathodic potential sweeps of CV across the reductive potential region. In addition, this finding is also consistent with a previous study by Ali Akbari *et al.* that the incorporation of $[\text{FeO}_4]^{2-}$ in KOH electrolyte into NiO_xH_y can be enhanced as the reduction potential becomes lower from 1.36 to $-0.14 V_{\text{RHE}}$ due to facile Fe adsorption on the electrode surface at low reduction potentials.²⁸ Also, Kuai *et al.* revealed that the intermittent reduction potential treatment can result in higher and more stable OER activity of NiFe-based electrocatalysts by revivifying the OER-inactive, segregated FeOOH to OER-active, Fe-incorporated NiO_xH_y . This implies the possibility that the cathodic sweeps across reduction potentials for Ni-CV may help prevent the undesired phase segregation of Fe and thus result in higher OER activity for Ni-CV compared with Ni-CP.⁶¹ However, Kuai *et al.* also reported in another study that the rate of Fe incorporation into nickel hydroxide is higher at OER potentials than at more negative potentials with respect to the $\text{Ni}^{2+/3+}$ redox peak potential, which is in contrast to our result.⁶² Given the fact that different materials (*in situ* formed NiO_xH_y obtained from electrochemical conditioning of Ni foil in this study and nickel hydroxide from the hydrothermal synthesis in Kuai *et al.*'s study) were compared for the study of Fe incorporation, it is speculated that different physicochemical properties (*e.g.*, crystallinity, crystal phase, porous structure, *etc.*) of initial materials before Fe incorporation could bring about different potential-dependent Fe incorporation characteristics, which necessitates further investigation.

2.2. Study of CP and CV Characteristics for NiSe Precatalysts on the FTO Substrate. Based on the fundamental understanding of CP and CV characteristics obtained from electrochemical conditioning of simple Ni foil, we extended our study to investigate the effects of CP and CV

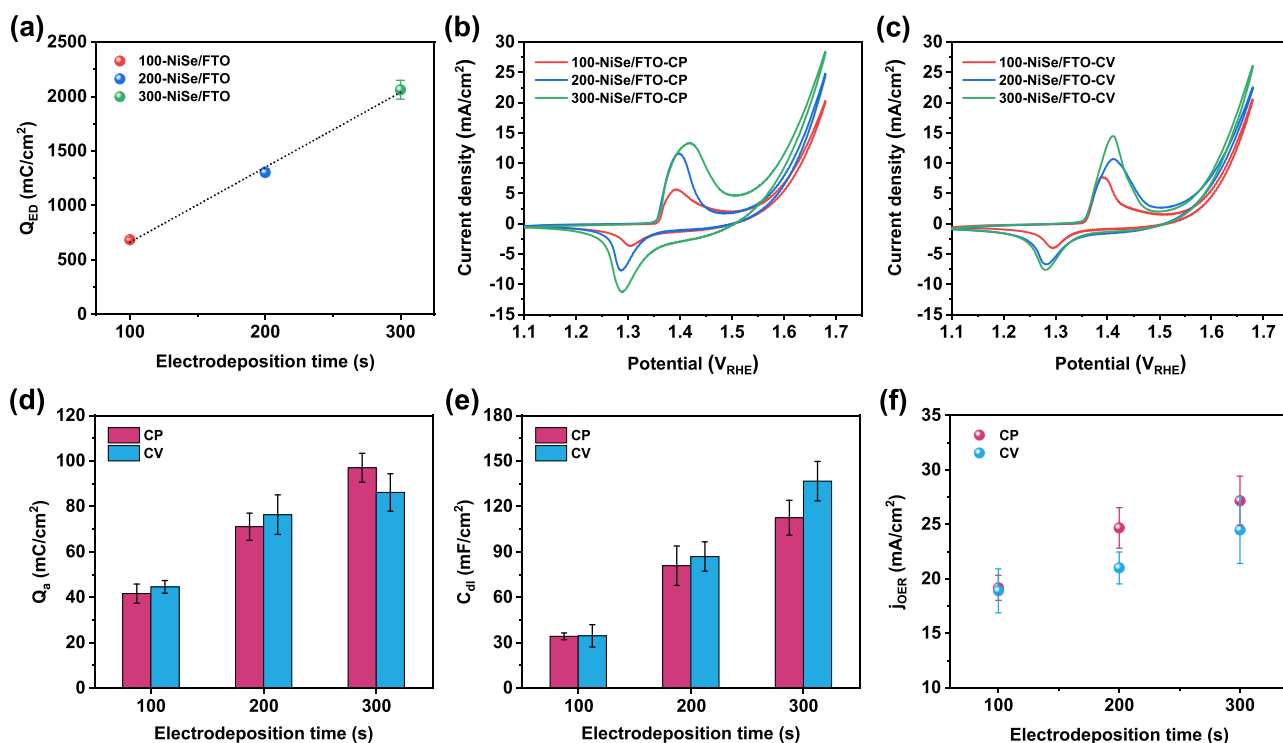


Figure 3. (a) Plot of Q_{ED} for x -NiSe/FTO with respect to electrodeposition time. (b–e) Electrochemical analyses of x -NiSe/FTO after CP and CV electrochemical conditioning in Fe-purified 1 M KOH electrolyte. CV curves at a scan rate of 10 mV/s of (b) x -NiSe/FTO-CP and (c) x -NiSe/FTO-CV. Plots of (d) Q_a and (e) C_{dl} from EIS at 1.68 V_{RHE} and (f) j_{OER} at 1.68 V_{RHE} with regard to electrodeposition time. Measurements were taken at least three times, and average values are presented with the standard error bar.

electrochemical conditioning for Ni-based compound precatalysts capable of efficient OER electrocatalysis. Considering the different degrees of *in situ* oxidation of OER precatalysts (e.g., partial or complete *in situ* oxidation) after random electrochemical conditioning in previous reports^{15–24} as well as the distinct characteristics of CP and CV studied in Section 2.1, it was hypothesized that the degree of *in situ* oxidation of OER precatalysts can be affected by the choice of electrochemical conditioning methods. Furthermore, it has been reported that transition metal compound precatalysts can form a porous and electrolyte-permeable structure as their anions dissolve into the electrolyte during *in situ* oxidation via electrochemical conditioning.^{11,33} Also, the *in situ* oxidation of OER precatalysts is accompanied by mass transport of reactants (OH[−]) to the surface and through the electrolyte-permeable bulk layer of precatalysts. Given these considerations, it was hypothesized that the degree of *in situ* oxidation can also be largely affected by the thickness of the precatalyst layer through which *in situ* oxidation should occur. To test these two hypotheses, nickel selenide was employed as an OER precatalyst for the study of CP and CV electrochemical conditioning of Ni-based compound precatalysts. The nickel selenide film was grown on FTO via electrodeposition. The electrodeposition condition was optimized to grow a uniform and single-phase nickel selenide film (Figures S11 and S12; see the Supporting Information for details related to the optimization of nickel selenide electrodeposition). Here, FTO was chosen as a substrate to solely investigate the effect of electrochemical conditioning on a nickel selenide film without interference from OER active substrates like Ni foil and Ni foam. Also, the thickness (or loadings) of the nickel selenide precatalysts on FTO was controlled by changing the

electrodeposition time to investigate the precatalyst thickness (or loading)-dependent CP and CV characteristics. Here, nickel selenide films that were grown on FTO using different electrodeposition times were denoted as x -NiSe/FTO, where x indicates 100, 200, or 300 s of electrodeposition time.

Figure S13 presents top-view SEM and EDX mapping images of x -NiSe/FTO. The SEM images show that each x -NiSe/FTO consists of nanoparticles with relatively uniform size and shape. Also, all the x -NiSe/FTO nanoparticles have a polyhedron shape, and the average particle size of 100-, 200-, and 300-NiSe/FTO were 308, 349, and 439 nm, respectively. The EDX mapping images show that for all the x -NiSe/FTO samples, nickel selenide was uniformly deposited on FTO in terms of their chemical composition. GIXRD analyses were performed to characterize the crystal structure of x -NiSe/FTO (Figure S14). All the x -NiSe/FTO exhibited peaks only corresponding to hexagonal NiSe and FTO, which signifies that a single phase of NiSe was successfully grown on the FTO. Moreover, XPS analyses for Ni 2p, Se 3d, and O 1s regions were conducted on the surface and in the bulk employing Ar⁺ sputtering of x -NiSe/FTO to examine their chemical composition and state. Figure S15 shows that pure NiSe with identical chemical compositions and states was successfully grown during the electrodeposition of x -NiSe/FTO (see the Supporting Information for details related to XPS analyses).

Figure S16 displays the chronoamperometry results at −0.51 V_{SCE} during electrodeposition of x -NiSe/FTO. It was observed that the current density of x -NiSe/FTO during electrodeposition, which indicates the rate of electrodeposition, was nearly constant among each sample, implying a well-controlled and reproducible electrodeposition condition. The Faradaic

charge that was passed during the electrodeposition of NiSe (Q_{ED}) was calculated to quantify the loadings of NiSe on FTO for different electrodeposition times (100–300 s). When Q_{ED} was plotted with respect to electrodeposition time, a linear trend was observed with an R^2 value of 0.997 (Figure 3a). This result suggests that by manipulating the electrodeposition time, the loading of NiSe film on FTO can be precisely controlled.

During CP and CV electrochemical conditioning of x -NiSe/FTO, the redox charge for $Ni^{2+/3+}$ transition and OER activity of x -NiSe/FTO increased because NiO_xH_y , which can act as an OER active species, was formed *via in situ* oxidation of NiSe (Figure S17). The electrochemical conditioning of x -NiSe/FTO was conducted until the OER activity and redox charge for $Ni^{2+/3+}$ were stabilized. Here, x -NiSe/FTO after CP and CV electrochemical conditioning was denoted as x -NiSe/FTO-CP and x -NiSe/FTO-CV, respectively. Figure 3b–f shows the electrochemical analysis results of x -NiSe/FTO-CP and x -NiSe/FTO-CV in Fe-purified 1 M KOH electrolyte. Note that in the Fe-purified KOH electrolyte, the effect of electrochemical conditioning on the degree of *in situ* oxidation of NiSe precatalysts can be studied independently of the effect of Fe incorporation, which is subject to the conditioning method used.

Figure 3d shows that Q_a increased with electrodeposition time for both x -NiSe/FTO-CP and x -NiSe/FTO-CV. This is because the amount of *in situ* formed NiO_xH_y was higher for the thicker NiSe layer with the longer electrodeposition time. However, when comparing the Q_a values of x -NiSe/FTO-CP and x -NiSe/FTO-CV with the same electrodeposition time, it was found that Q_a could have different values depending on the electrochemical conditioning method. 100-NiSe/FTO-CP and 100-NiSe/FTO-CV had almost identical Q_a values, but 200-NiSe/FTO-CV had a higher Q_a value than 200-NiSe/FTO-CP, implying the possibility that CV can result in a higher degree of *in situ* oxidation for thicker NiSe samples compared to CP. However, 300-NiSe/FTO-CV had a lower Q_a value than 300-NiSe/FTO-CP.

Together with Q_a , C_{dl} is another parameter that can indicate the degree of *in situ* oxidation of the NiSe precatalyst, because as NiSe layers are *in situ* oxidized, it forms a porous and electrolyte-permeable structure that can have a larger surface area exposed to the electrolyte and, thus, a higher C_{dl} value.^{11,33} To obtain the C_{dl} values, EIS analysis was conducted at 1.68 V_{RHE} . Figure S18 displays the Bode and Nyquist plots of the EIS spectra of x -NiSe/FTO-CP and x -NiSe/FTO-CV. Notably, Figure S18c,f shows that the semicircles of Nyquist plots at lower frequencies had asymmetrical shapes due to electron transport resistance through the porous catalyst layer,^{33,63–65} which is in line with the formation of the porous structure of OER precatalyst during electrochemical activation. It is noted that the contribution of mass transport of OH^- to the asymmetrical shape of the Nyquist plot is negligible (see the Supporting Information and Figure S19 for a detailed explanation). EIS data were fitted employing the transmission line model in Figure S3b and the corresponding equivalent circuit model in Figure S3c, and the obtained parameters were summarized in Table S4 (see the Supporting Information for details related to EIS analysis). Similar to Q_a , C_{dl} also increased with electrodeposition time for both x -NiSe/FTO-CP and x -NiSe/FTO-CV (Figure 3e). When comparing the C_{dl} values of x -NiSe/FTO-CP and x -NiSe/FTO-CV with the same electrodeposition time, 100-NiSe/FTO-CP and 100-NiSe/FTO-CV had almost identical C_{dl} values. On the other hand, 200- and

300-NiSe/FTO-CV had higher C_{dl} values than 200- and 300-NiSe/FTO-CP. This result indicates that 200- and 300-NiSe/FTO-CV experienced a higher degree of *in situ* oxidation than 200- and 300-NiSe/FTO-CP, respectively. The trend of Q_a and C_{dl} with respect to the electrochemical conditioning method and electrodeposition time were consistent except that 300-NiSe/FTO-CV had a smaller Q_a value than 300-NiSe/FTO-CP, which will be further discussed later.

To better understand the degree of *in situ* oxidation of x -NiSe/FTO-CP and x -NiSe/FTO-CV that is deduced from the above Q_a and C_{dl} results, post-OER material characterizations for x -NiSe/FTO-CP and x -NiSe/FTO-CV were conducted. To check whether any NiSe remained within the NiSe precatalyst layer after electrochemical conditioning, GIXRD analysis was performed. Figure 4 shows that x -NiSe/FTO-CV

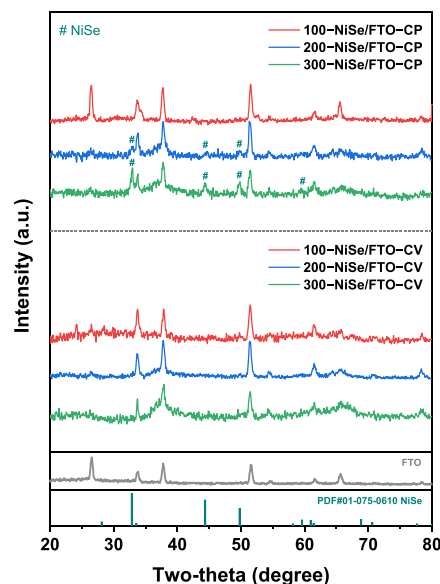


Figure 4. GIXRD spectra of x -NiSe/FTO-CP and x -NiSe/FTO-CV.

samples do not exhibit any peaks corresponding to NiSe. This finding indicates that the entire NiSe layer was completely oxidized during CV electrochemical conditioning and was transformed into amorphous NiO_xH_y or a trace amount of nanocrystalline NiO_xH_y , that is not detected by GIXRD. As for x -NiSe/FTO-CP, 100-NiSe/FTO-CP did not exhibit any peaks corresponding to NiSe, while 200-NiSe/FTO-CP exhibited small peaks corresponding to NiSe and 300-NiSe/FTO-CP exhibited even more intense peaks. This result suggests that the relatively thin NiSe precatalyst layer of 100-NiSe/FTO-CP was completely *in situ* oxidized, whereas the thicker NiSe precatalyst layer of 200- and 300-NiSe/FTO-CP underwent partial *in situ* oxidation and retained NiSe together with *in situ* formed amorphous or a trace amount of nanocrystalline NiO_xH_y .

To further probe how *in situ* oxidation occurs through the NiSe precatalyst layer, the chemical composition across the NiSe precatalyst layer after electrochemical conditioning was investigated by XPS analyses on the surface and in the bulk employing Ar^+ sputtering. Figure S20 indicates that *in situ* oxidation occurred throughout the entire NiSe layer for all the x -NiSe/FTO-CP and x -NiSe/FTO-CV. However, while x -NiSe/FTO-CV and 100-NiSe/FTO-CP underwent complete *in situ* oxidation, 200- and 300-NiSe/FTO-CP underwent

partial *in situ* oxidation, leaving the NiSe and NiO_xH_y, together within the bulk NiSe layer. Moreover, it was found that 300-NiSe/FTO-CP with a thicker NiSe layer maintained more NiSe than 200-NiSe/FTO-CP (see the Supporting Information for details related to XPS analyses).

Although the above post-OER GIXRD and XPS analyses provided insight into how *in situ* oxidation occurred across the entire NiSe layer, it is still unclear how each NiSe particle in the NiSe precatalyst layer was transformed during electrochemical conditioning. To further investigate how *in situ* oxidation occurs on NiSe particles depending on the electrochemical conditioning method, 300-NiSe/FTO-CP and 300-NiSe/FTO-CV obtained from the same 300-NiSe/FTO and with the most distinct *in situ* oxidation features according to GIXRD and XPS analyses were selected for further study. Also, the partial and complete *in situ* oxidation of 300-NiSe/FTO-CP and 300-NiSe/FTO-CV were further confirmed by EDX mapping and spectrum analyses. Figures S21c,d and S22c,d suggest that a significant amount of Se remained in 300-NiSe/FTO-CP while almost no Se remained in 300-NiSe/FTO-CV, which are consistent with GIXRD and XPS results.

Transmission electron microscopy (TEM) images and selected area electron diffraction (SAED) patterns for 300-NiSe/FTO-CP and 300-NiSe/FTO-CV were measured to probe the transformation of NiSe particles after electrochemical conditioning. The TEM image in Figure 5a indicates

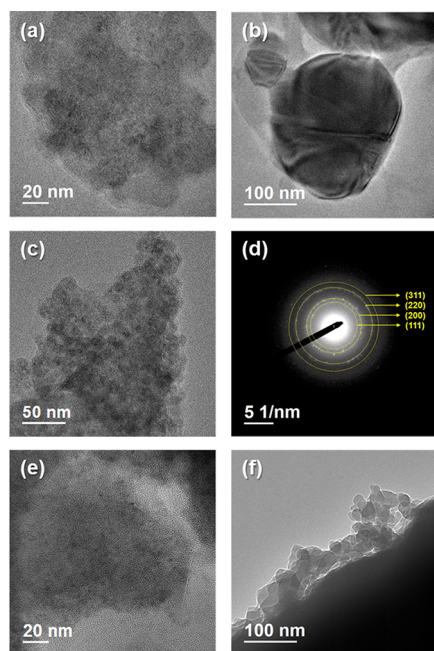


Figure 5. (a–c) TEM images and (d) SAED pattern from (c) of 300-NiSe/FTO-CP. (e, f) TEM images of 300-NiSe/FTO-CV.

that 300-NiSe/FTO-CP contains amorphous NiO_xH_y with no clear lattice fringes. The large chunk-like particles in Figure 5b are remaining NiSe particles that are not fully oxidized in 300-NiSe/FTO-CP. Figure 5c shows additional nanoparticle products with ~10 nm in size, and their corresponding SAED patterns in Figure 5d display the four main diffraction ring patterns matching with the (111), (200), (220), and (311) planes of cubic NiO,⁶⁶ which indicates that nanocrystalline NiO was also formed for 300-NiSe/FTO-CP. On the

other hand, the TEM images for 300-NiSe/FTO-CV in Figure 5e,f only show the amorphous NiO_xH_y with no clear lattice fringes. Large chunk-like particles or nanocrystals are not observed due to the complete *in situ* oxidation of 300-NiSe/FTO-CV. To better identify the large chunk-like particles in 300-NiSe/FTO-CP shown in Figure 5b, bright-field scanning transmission electron microscopy (STEM) and EDX mapping analysis were performed. Figure 6a,b presents that the big chunk particle consists of a dark core and a bright shell. EDX mapping images in Figure 6c–f further demonstrate that this core–shell particle consists of a NiSe core and *in situ* oxidized NiO_xH_y shell.

Furthermore, the morphology of NiO_xH_y *in situ* formed via CP and CV electrochemical conditioning of NiSe was compared using SEM analyses (Figures S21a,b and S22a,b). Given that the NiSe on the top surface of both 300-NiSe/FTO-CP and 300-NiSe/FTO-CV were completely oxidized according to XPS analyses in Figure S20a–c, the top-view SEM images of each sample were expected to exhibit NiO_xH_y with similar morphology. Interestingly, however, it was found that *in situ* formed NiO_xH_y had different morphologies depending on the electrochemical conditioning method. Figure S21a,b shows that 300-NiSe/FTO-CP seemed to grow stacks of NiO_xH_y platelets on the surface. On the other hand, for 300-NiSe/FTO-CV, NiSe particles cracked and shattered into aggregates of NiO_xH_y after CV electrochemical conditioning (Figure S22a,b), which is similar to the structural transformation (e.g., cracking and restructuring) of NiO_xH_y after CV electrochemical conditioning in the previous study.⁶⁷

The above post-OER material characterizations (GIXRD, XPS, SEM, EDX, TEM, SAED, and STEM) indicate that CP and CV electrochemical conditioning of NiSe precatalyst results in different material properties including *in situ* oxidized layer thickness, chemical composition, crystallinity, and morphology. Specifically, CV electrochemical conditioning resulted in complete *in situ* oxidation of the NiSe layers of *x*-NiSe/FTO, forming randomly shattered aggregates of amorphous NiO_xH_y regardless of the thickness of NiSe layer. On the other hand, CP electrochemical conditioning resulted in complete *in situ* oxidation for a relatively thin NiSe layer of 100-NiSe/FTO but partial *in situ* oxidation for the thicker NiSe layer of 200- and 300-NiSe/FTO. In particular, the degree of *in situ* oxidation changed with the depth of the NiSe layer for 200- and 300-NiSe/FTO-CP: complete oxidation on the top surface and partial oxidation in the bulk. As a result, it forms stacked platelets of amorphous NiO_xH_y, nanocrystalline NiO, and core–shell particles consisting of a NiSe core covered by an *in situ* oxidized shell. It appears that the different degree of *in situ* oxidation of *x*-NiSe/FTO-CP and *x*-NiSe/FTO-CV is related to their different electrolyte-permeable thicknesses, which are determined by the electrochemical conditioning method. According to the results of the electrochemical conditioning of Ni foil in Section 2.1, CV with cathodic potential sweeps is more favorable than CP for the electrolyte to penetrate to the deeper side of the Ni layer, creating a thicker hydrous NiO_xH_y layer. In the same way, CV electrochemical conditioning likely creates more channels for the electrolyte to permeate through the entire NiSe layer compared to CP and thus results in complete *in situ* oxidation of the entire NiSe precatalyst layer. Similarly, in terms of crystallinity and morphology, CV electrochemical conditioning, which facilitates rearrangement of oxyanion species (*i.e.*, NiO_xH_y) into a disrupted state *via* reductive oxidation and

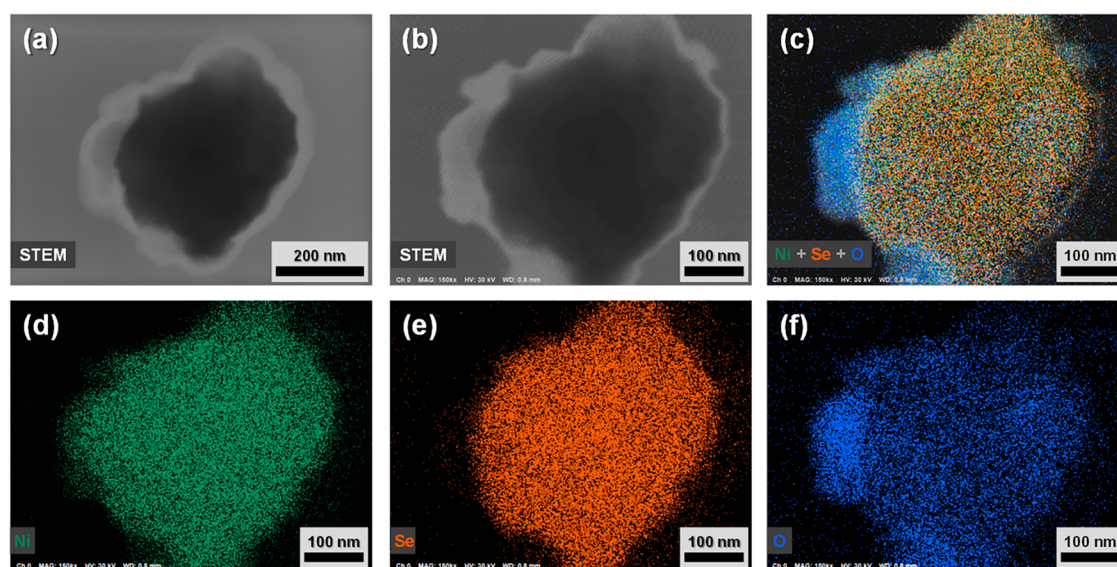


Figure 6. (a, b) Bright-field STEM and (c–f) EDX mapping images of 300-NiSe/FTO-CP.

reduction,^{39,67} is likely to transform any crystalline and well-structured NiO_xH_y to amorphous and randomly shattered NiO_xH_y .

The interpretation of the degree of *in situ* oxidation of x -NiSe/FTO-CP and x -NiSe/FTO-CV based on electrochemical analyses (Q_a and C_{dl}) and material characterizations was consistent except that 300-NiSe/FTO-CV, which experienced complete *in situ* oxidation, had a smaller Q_a value than 300-NiSe/FTO-CP, which underwent partial *in situ* oxidation. This exception can be explained by a previous study in which the measured Q_a value for a thicker NiO_xH_y film with electron transport limitations could be underestimated due to the irreversible trapping of a portion of redox-active Ni sites in the oxidized state.⁴¹ To summarize, the electrochemical analysis results (Q_a and C_{dl}) also suggest that CV electrochemical conditioning results in complete *in situ* oxidation of thicker NiSe layers (200- and 300-NiSe/FTO), while CP electrochemical conditioning results in their partial *in situ* oxidation.

Figure 3f shows that the OER activity of x -NiSe/FTO-CP and x -NiSe/FTO-CV increased as their active surface area based on C_{dl} increased with the electrodeposition time. The 100-NiSe/FTO-CP and 100-NiSe/FTO-CV samples exhibited almost identical OER activity because they both underwent complete *in situ* oxidation and, as a result, had nearly identical active surface areas. On the other hand, 200- and 300-NiSe/FTO-CP exhibited higher OER activity than 200- and 300-NiSe/FTO-CP despite their smaller active surface area compared to 200- and 300-NiSe/FTO-CV. This is because the metallic NiSe, which could contribute to the superb intrinsic activity *via* synergistic electronic effects between NiSe and the NiO_xH_y layer and electrical conductivity, remained in 200- and 300-NiSe/FTO-CP as opposed to 200- and 300-NiSe/FTO-CV without any remaining NiSe. This OER activity trend offers the insight that complete *in situ* oxidation of OER precatalysts *via* electrochemical conditioning to achieve the largest active surface area does not necessarily guarantee the best OER performance.

2.3. Study of CP and CV Characteristics for NiSe Precatalysts on Ni Foil Substrate. Ni-based substrates (e.g., Ni foam and Ni foil) have been widely employed as substrates for OER precatalysts.^{28–32} So far, when measuring and

interpreting the OER performance, the contribution of Ni-based substrates to OER electrocatalysis has rarely been considered. However, considering that *in situ* oxidation can occur throughout the entire OER precatalyst layer during electrochemical conditioning as discussed in Section 2.2 and Ni is an OER active material, it is possible that Ni-based substrates for OER precatalysts are exposed to the electrolyte, electrochemically conditioned, and involved in the OER. Furthermore, based on the distinct electrochemical analysis results (e.g., Q_a , C_{dl} , and j_{OER}) of Ni foil after CP and CV electrochemical conditioning in Section 2.1, it is hypothesized that depending on the electrochemical conditioning method, how Ni-based substrates affect the electrochemical characteristics and OER activity of precatalysts on Ni-based substrates may vary. To test these hypotheses, NiSe films were grown on Ni foil substrate *via* electrodeposition for 100 s, electrochemically conditioned employing CP and CV, and denoted as 100-NiSe/Ni-CP and 100-NiSe/Ni-CV. The electrochemical analyses of 100-NiSe/Ni-CP and 100-NiSe/Ni-CV were conducted in both Fe-purified and Fe-unpurified 1 M KOH electrolytes. The effect of Ni-based substrate on electrochemical characteristics and OER activity of 100-NiSe/Ni-CP and 100-NiSe/Ni-CV was examined by comparing them with Ni-CP, Ni-CV, 100-NiSe/FTO-CP, and 100-NiSe/FTO-CV.

Figure 7a–d shows the electrochemical analysis results of 100-NiSe/Ni-CP and 100-NiSe/Ni-CV in Fe-purified 1 M KOH electrolyte, and Figure S23 shows their comparison with 100-NiSe/FTO-CP and 100-NiSe/FTO-CV. The Q_a and cathodic charge (Q_c) for the redox reaction of $\text{Ni}^{2+/3+}$ of 100-NiSe/Ni-CV were higher than those of 100-NiSe/Ni-CP (Figure 7b,c).

Given that 100-NiSe/FTO-CP and 100-NiSe/FTO-CV experienced complete *in situ* oxidation of the NiSe layers and had almost the same Q_a value, the difference in Q_a and Q_c between 100-NiSe/Ni-CP and 100-NiSe/Ni-CV is related to the Ni foil substrate, not the oxidized NiSe layer (Figure S23a). Moreover, considering the higher Q_a and C_{dl} of Ni-CV compared to Ni-CP (Figure 1b,c,f,g), it is inferred that the Ni foil substrate of 100-NiSe/Ni-CV that was electrochemically conditioned *via* CV created a relatively thick NiO_xH_y layer with higher Q_a and Q_c values, while that of 100-NiSe/Ni-CP

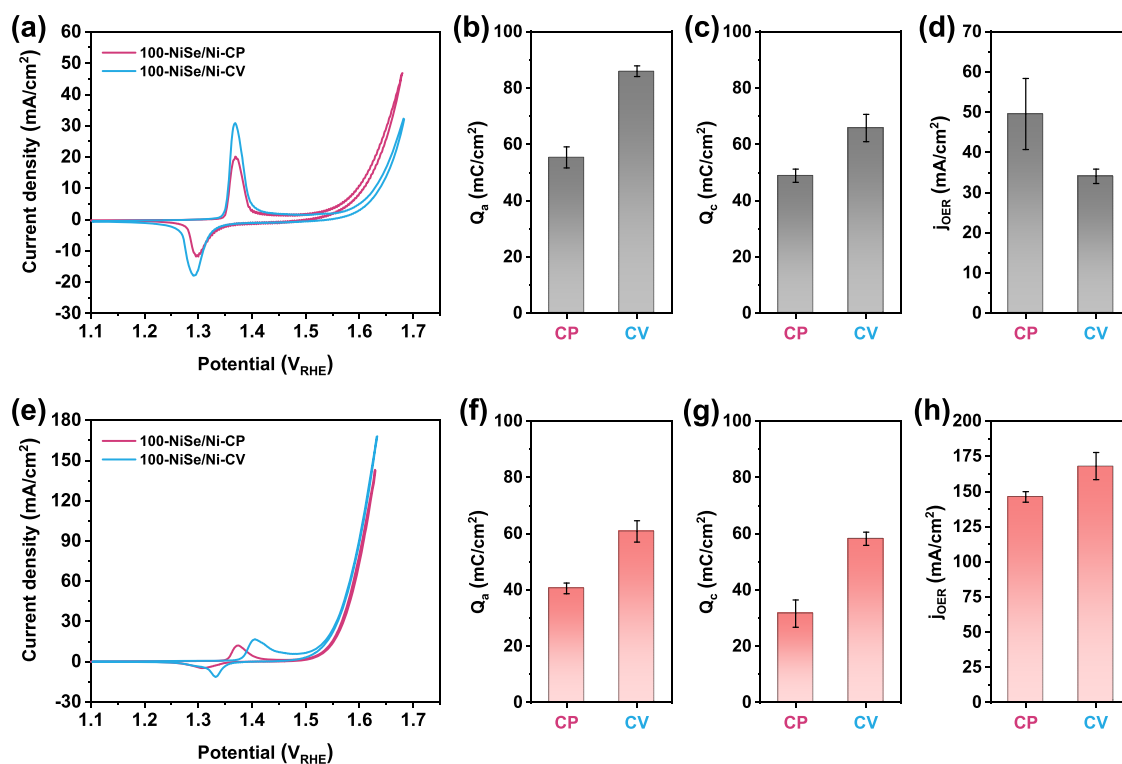


Figure 7. Electrochemical analyses of 100-NiSe/Ni-CP and 100-NiSe/Ni-CV in (a–d) Fe-purified and (e–h) Fe-unpurified 1 M KOH electrolytes. (a) CV curves at a scan rate of 10 mV/s, (b) Q_a , (c) C_{dl} from EIS at 1.68 V_{RHE} , and (d) j_{OER} at 1.68 V_{RHE} . (e) CV curves at a scan rate of 10 mV/s, (f) Q_a , (g) C_{dl} from EIS at 1.68 V_{RHE} , and (h) j_{OER} at 1.68 V_{RHE} . Measurements were taken at least three times, and average values are presented with the standard error bar.

that was electrochemically conditioned *via* CP created a relatively thin NiO_xH_y layer with lower Q_a and Q_c values. Collectively, these results suggest that the difference in Q_a and Q_c values between 100-NiSe/Ni-CP and 100-NiSe/Ni-CV originated from the difference in Q_a and Q_c values between the Ni foil substrates of 100-NiSe/Ni-CP and 100-NiSe/Ni-CV. Figure 7d presents the OER activity of 100-NiSe/Ni-CP and 100-NiSe/Ni-CV. It is noted that the OER activities of 100-NiSe/Ni-CP and 100-NiSe/Ni-CV were higher than those of 100-NiSe/FTO-CP and 100-NiSe/FTO-CV (Figure S23b). This is related to the superb electrical conductivity of Ni foil, better adhesion of NiSe on the Ni foil substrate compared to FTO, and better contact between the Ti clip and the thin Ni foil compared to between the Ti clip and the thick FTO. Moreover, while 100-NiSe/FTO-CP and 100-NiSe/FTO-CV had the same OER activity, 100-NiSe/Ni-CV exhibited lower OER activity than 100-NiSe/Ni-CP. This result implies that this OER activity difference is associated with the Ni foil substrate that was electrochemically conditioned differently rather than the NiSe layer. Given the Q_a trend, the lower OER activity of 100-NiSe/Ni-CV compared to 100-NiSe/Ni-CP is attributed to a greater electron transport limitation for 100-NiSe/Ni-CV with a thicker NiO_xH_y layer from the Ni foil substrate compared to 100-NiSe/Ni-CP with a thinner NiO_xH_y layer from the Ni foil substrate, as in the case of Ni-CP and Ni-CV in Section 2.1.

Figure 7e–h shows the electrochemical analysis results of 100-NiSe/Ni-CP and 100-NiSe/Ni-CV in Fe-unpurified 1 M KOH electrolyte. From the CV curves in Figure 7e, the redox peaks for the $Ni^{2+/3+}$ transition of 100-NiSe/Ni-CP and 100-NiSe/Ni-CV were positively shifted compared to those in Fe-purified KOH electrolyte in Figure 7a, implying successful Fe

incorporation into the NiO_xH_y layer during electrochemical conditioning. Similar to the trend of Q_a and Q_c in Fe-purified electrolyte, the Q_a and Q_c of 100-NiSe/Ni-CV were higher than those of 100-NiSe/Ni-CP (Figure 7f,g). It is noted that Q_a and Q_c values in the Fe-unpurified electrolyte were smaller than those in the Fe-purified electrolyte due to the suppression of the $Ni^{2+/3+}$ redox reaction in the presence of Fe in NiO_xH_y .^{33,57,58} Figure 7h shows that the OER activity of 100-NiSe/Ni-CV was higher than that of 100-NiSe/Ni-CP, which is reverse to their OER activities in the Fe-purified electrolyte in Figure 7d. Since this reverse OER activity trend in the Fe-unpurified electrolyte is associated with the incorporation of Fe impurities from the KOH electrolyte into the NiO_xH_y layer, Fe composition and its effect on OER activity of 100-NiSe/Ni-CP and 100-NiSe/Ni-CV were investigated.

From the CV curves in Figure 7e, the redox peaks for 100-NiSe/Ni-CV were more positively shifted than those for 100-NiSe/Ni-CP, implying a higher degree of Fe incorporation into 100-NiSe/Ni-CV compared to 100-NiSe/Ni-CP. The difference in Fe incorporation was further confirmed by XPS analysis of NiO_xH_y layers derived from NiSe precatalyst layers. The Fe compositions of 100-NiSe/Ni-CP and 100-NiSe/Ni-CV were 11.6 and 16.4%, respectively (Table S5), both of which, however, are in the optimal Fe composition range of 10–25% to show the best OER performance.^{13,14} To comprehend the influence of intrinsic activity and transport limitation on the OER activity, the Tafel slope was investigated (Figure S24). The Tafel slopes of 100-NiSe/Ni-CV (77.4 mV and 121 mV dec^{-1}) were higher than those of 100-NiSe/Ni-CP (57.9 and 110 mV dec^{-1}), indicating that 100-NiSe/Ni-CV had lower OER kinetics as a result of its intrinsic activity and transport limitation. Thus, it is understood that the larger

Scheme 1. Schematic Illustration of Ni Foil, NiSe/FTO, and NiSe/Ni Foil before and after CP and CV Electrochemical Conditioning that Shows the Different Degrees of *In Situ* Oxidation Depending on the Electrochemical Conditioning Method

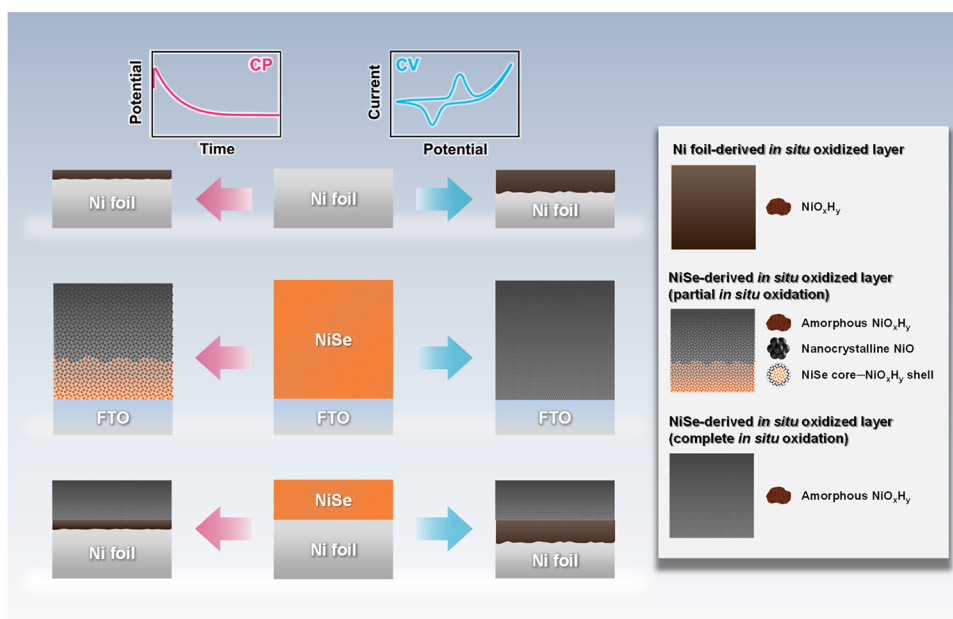


Table 1. A Summary and Comparison of Characteristics of CP and CV Electrochemical Conditioning Methods

method	<i>in situ</i> oxidation	Fe incorporation	characteristics
CP	medium	medium	<ol style="list-style-type: none"> 1. Partial <i>in situ</i> oxidation can occur for thick OER precatalysts due to the thin electrolyte-permeable thickness. 2. Transition metal compound cores and oxidized shells, which can have a synergistic electronic effect and good electrical conductivity, can be maintained. 3. Ni-based substrates do not significantly affect the OER characteristics. 4. Fe incorporation mainly occurs near the surface of NiO_xH_y layer.
CV	high	high	<ol style="list-style-type: none"> 1. Complete <i>in situ</i> oxidation can occur for thick OER precatalysts due to the thick electrolyte-permeable thickness. 2. Large active surface area can be achieved. 3. Synergistic electronic effect and good electrical conductivity from transition metal compound precatalysts can be lost. 4. Ni-based substrates can be involved in OER characteristics. 5. Fe incorporation can occur in the deeper side of the NiO_xH_y layer.

active surface area of 100-NiSe/Ni-CV, which originates from Fe-doped NiO_xH_y layer created from a Ni foil substrate, results in its higher OER activity despite its lower kinetics compared to 100-NiSe/Ni-CP. Collectively, it is concluded not only that the Ni substrate of 100-NiSe/Ni can be *in situ* oxidized during electrochemical conditioning but also that the *in situ* oxidized Ni substrate can affect the electrochemical characteristics (e.g., active surface area, electron transport, etc.) and OER activity differently depending on the electrochemical conditioning method; for example, the involvement of Ni-based substrates in OER would be smaller for CP electrochemical conditioning than for CV electrochemical conditioning.

Additionally, regarding the degree of Fe incorporation, it is worth noting that in the Fe-unpurified electrolyte, the Fe compositions in 100-NiSe/Ni-CP and 100-NiSe/Ni-CV were higher than those in Ni-CP and Ni-CV. This different degree of Fe incorporation after identical electrochemical conditioning is likely associated with their different NiO_xH_y material properties. The NiO_xH_y layer derived from the NiSe precatalyst layer can have porous morphology with more defect/edge sites that are favorable for Fe incorporation in comparison with the NiO_xH_y layer derived from a Ni foil substrate.^{3,57,59–62} Also, it was observed that the Fe composition of 100-NiSe/Ni-CV was higher than that of

100-NiSe/Ni-CP as the Fe composition of Ni-CV was higher than that of Ni-CP. This finding again confirms that CV with both anodic and cathodic potential sweeps is more favorable for Fe incorporation than CP with only anodic potential applied. Collectively, these results suggest that both NiO_xH_y material properties and the electrochemical conditioning method can play a key role in determining the degree of Fe incorporation into the NiO_xH_y layer.

3. CONCLUSIONS

In this study, we investigated the effects of CP and CV electrochemical conditioning on Ni-based OER electrocatalysts by changing the composition (e.g., Ni and NiSe) and thickness of the electrocatalysts, the type of substrate (e.g., FTO and Ni foil), and the electrolyte (e.g., Fe-purified and Fe-unpurified KOH). Thorough electrochemical analyses and material characterizations revealed that the degree of *in situ* oxidation and Fe incorporation of OER electrocatalysts can change depending on the electrochemical conditioning method, thereby resulting in different material properties (e.g., *in situ* oxidized layer thickness, chemical composition, crystallinity, and morphology), which is illustrated in Scheme 1, and electrochemical parameters (e.g., Q_a , Q_c , and C_{dl}) and characteristics (e.g., active surface area, electron transport

limitation, and intrinsic activity). This difference can not only influence the overall OER activity but also complicate its interpretation and comparison between samples. Depending on the intent of a study, whether it may be to achieve high performance or to make a fair activity comparison among various electrocatalysts, it is recommended to choose the proper electrochemical conditioning method for electrochemical activation or long-term stability tests by considering the distinct effects of electrochemical conditioning methods summarized in Table 1.

4. EXPERIMENTAL SECTION

4.1. Materials and Chemicals. Ni foil with a thickness of 0.25 mm and a purity of 99.5% (Alfa Aesar), FTO glass (TEC 7, Sigma-Aldrich), and potassium hydroxide (90% flakes, Sigma-Aldrich) were used. Ethanol (99.5%, PHARMCO), deionized (DI) water ($> 18 \text{ M}\Omega \text{ cm}$ resistivity), selenium(IV) oxide (99.999%, Acros Organics), nickel chloride (98%, Acros Organics), lithium chloride (anhydrous, Acros Organics), nickel nitrate hexahydrate (99%, Acros Organics), and hydrochloric acid (Fisher Scientific) were used without further purification.

4.2. Electrodeposition of NiSe Film on FTO Glass and Ni Foil Substrates. FTO glass was ultrasonically cleaned using ethanol and DI water for 10 min each and dried with compressed air. The surface of the FTO glass was masked using a 3M 470 electroplating tape, and a geometric area of $\sim 0.5 \text{ cm}^2$ of FTO was left exposed. Ni foil was ultrasonically cleaned using ethanol and DI water for 10 min each. Additionally, right before electrodeposition, Ni foil was sonicated in 1 M HCl for 10 min to remove surface nickel oxide formed due to air exposure and rinsing with DI water. The backside of the Ni foil was masked using a 3M 470 electroplating tape before electrodeposition to prevent the deposition of nickel selenide onto the backside of the Ni foil. A solution for electrodeposition was prepared by dissolving 65 mM NiCl_2 , 10 mM SeO_2 , and 100 mM LiCl in DI water and stirring the solution for 6 h at 25 °C. For electrodeposition, a saturated calomel electrode (SCE) and a graphite electrode were used as the reference and counter electrodes, respectively. Linear sweep voltammetry (LSV) and chronoamperometry (CA) techniques with 85% of iR drop compensation were used for the electrodeposition of NiSe film on FTO glass and Ni foil substrates. The electrodeposition condition was optimized to grow a uniform and single-phase NiSe film (see the Supporting Information for details related to the optimization of electrodeposition conditions). First, one LSV from 0 to -0.75 V (vs SCE, V_{SCE}) was conducted without stirring as pretreatment, and then CA was carried out at $-0.51 V_{\text{SCE}}$ with stirring. The thickness of the NiSe film was controlled by changing the electrodeposition time (100, 200, and 300 s). After electrodeposition, NiSe films on substrates were carefully rinsed with DI water, dried with compressed air, and stored under ambient conditions. The backsides of the as-prepared NiSe/Ni samples were masked using polydimethylsiloxane (PDMS) before electrochemical analyses to prevent the exposure of pure Ni foil to the electrolyte.

4.3. Physicochemical Characterizations. Top-view SEM images and EDX analysis results were obtained using FEI Quanta 650 ESEM at an accelerating voltage of 10 kV and under a vacuum of approximately 5×10^{-6} Torr. The crystal structure of Ni-CP, Ni-CV, and NiSe/FTO samples before and after OER electrochemical conditioning was characterized by

grazing incidence X-ray diffraction (GIXRD, Ultima IV Diffractometer, Rigaku) equipped with Cu K_{α} radiation ($\lambda = 1.54186 \text{ \AA}$) using 40 kV of generator voltage and 44 mA. For the GIXRD analyses, thin-film configuration and incident angle of 0.3° were used. Raman spectra of Ni-CP and Ni-CV were collected using a Horiba LabRAM HR Evolution instrument using a $\times 100$ microscope objective and a laser with a 633 nm wavelength. Surface and bulk chemical compositions and functionalities of NiSe/FTO samples before and after OER electrochemical conditioning were characterized by XPS (Axis Ultra DLD spectrometer, Kratos) using monochromatic Al K_{α} radiation (1486.6 eV) with a spot size of 400 μm and an Ar^+ sputter. Also, XPS analysis using Mg K_{α} radiation (1253.6 eV) was performed for Ni foil and NiSe/Ni samples after OER electrochemical conditioning in the Fe-unpurified KOH electrolyte to detect the relatively low concentration of Fe in NiO_xH_y , by avoiding the overlapping of Ni LMM Auger features with the Fe 2p peaks from the Al radiation source. All binding energies were adjusted to the adventitious carbon C 1s signal at 284.8 eV. The TEM images and SAED patterns were obtained using JEOL 2010F with a voltage of 200 kV and a camera length of 40 cm. STEM images and the corresponding elemental mapping images were obtained by using a Hitachi S5500 SEM that operates in the STEM mode with an accelerating voltage of 30 kV as well as with a Bruker XFlash EDX detector attachment at 5 kV. The Fe concentrations in 1 M Fe-purified and Fe-unpurified KOH electrolytes were analyzed through solution-mode ICP-MS using an Agilent 7500ce equipped with a collision reaction cell (He and H_2 modes).

4.4. Electrochemical Measurements. Electrochemical analyses were carried out in Fe-purified or Fe-unpurified 1 M KOH electrolyte depending on the samples. An aqueous solution of 1 M KOH was prepared by dissolving KOH solid salts in ultrapure DI water. For the preparation of the Fe-purified 1 M KOH electrolyte, 1 M KOH solution was purified according to the previous method using the absorption of Fe by $\text{Ni}(\text{OH})_2$.¹¹ A polypropylene container was washed with 0.5 M H_2SO_4 and DI water to remove any remaining impurities and then employed as an electrochemical reactor to avoid any possible contamination (e.g., glass-etching in alkaline media). A Teflon-coated titanium (Ti) clip was used as a working electrode to connect the sample to a potentiostat. Electrochemical analyses were conducted using a CHI660D electrochemical workstation (CH Instrument, USA) with a three-electrode configuration. A graphite rod and Hg/HgO in 1 M KOH served as counter and reference electrodes, respectively. The potential applied to the Hg/HgO reference electrode ($E_{\text{Hg}/\text{HgO}}$) was converted into the reversible hydrogen electrode (RHE) scale via the Nernst equation [$E_{\text{RHE}} = E_{\text{Hg}/\text{HgO}} + 0.059 \times \text{pH} + E_{\text{Hg}/\text{HgO}}^\circ$], where $E_{\text{Hg}/\text{HgO}}^\circ$ in 1 M KOH at 25 °C is 0.098 V. The 85% iR drop from uncompensated resistance (R_u) was compensated during CV for OER measurements. However, during the electrochemical conditioning using CP and CV, the iR drop was not compensated. CP and CV electrochemical conditioning were conducted until there was no significant change (i.e., stabilization) in OER activity or redox charge for $\text{Ni}^{2+/3+}$ in the subsequent CV measurements. The CV analyses for Ni foil were conducted at a scan rate of 20 mV/s in the potential range of 1.10–1.63 V_{RHE} , while the CV analyses for NiSe/FTO and NiSe/Ni samples were performed at a scan rate of 10 mV/s in the potential range of 1.10–1.68 V_{RHE} . EIS was measured

in the frequency range from 5×10^{-2} to 10^6 Hz with 10 mV of amplitude at 1.63 V_{RHE} for Ni foil and 1.68 V_{RHE} for NiSe/FTO and NiSe/Ni samples. All electrochemical analyses and conditioning were conducted with the stirring of the magnetic bar.

■ ASSOCIATED CONTENT

SI Supporting Information

The Supporting Information is available free of charge at <https://pubs.acs.org/doi/10.1021/acscatal.2c01001>.

Optimization of electrodeposition of NiSe; CP and CV for electrochemical conditioning, scan-rate dependent CVs, Tafel slopes, EIS spectra, equivalent circuit models for EIS fitting, and CV using rotating disk electrode; additional material characterization results such as ICP-MS, XPS, SEM, EDX, Raman spectra, and GIXRD (PDF)

■ AUTHOR INFORMATION

Corresponding Author

C. Buddie Mullins – McKetta Department of Chemical Engineering, Department of Chemistry, Center for Electrochemistry, and H2@Scale Project, The University of Texas at Austin, Austin, Texas 78712, United States; Texas Materials Institute, The University of Texas at Austin, Austin, Texas 78712, United States; orcid.org/0000-0003-1030-4801; Email: mullins@che.utexas.edu

Authors

Yoon Jun Son – McKetta Department of Chemical Engineering, The University of Texas at Austin, Austin, Texas 78712, United States; orcid.org/0000-0003-1704-2314

Seonwoo Kim – McKetta Department of Chemical Engineering, The University of Texas at Austin, Austin, Texas 78712, United States

Vanessa Leung – McKetta Department of Chemical Engineering, The University of Texas at Austin, Austin, Texas 78712, United States

Kenta Kawashima – Department of Chemistry, The University of Texas at Austin, Austin, Texas 78712, United States; orcid.org/0000-0001-7318-6115

Jungchul Noh – McKetta Department of Chemical Engineering, The University of Texas at Austin, Austin, Texas 78712, United States

Kihoon Kim – McKetta Department of Chemical Engineering, The University of Texas at Austin, Austin, Texas 78712, United States

Raul A. Marquez – Department of Chemistry, The University of Texas at Austin, Austin, Texas 78712, United States; orcid.org/0000-0003-3885-5007

Omar A. Carrasco-Jaim – McKetta Department of Chemical Engineering, The University of Texas at Austin, Austin, Texas 78712, United States

Lettie A. Smith – Department of Chemistry, The University of Texas at Austin, Austin, Texas 78712, United States; orcid.org/0000-0003-0378-072X

Hugo Celio – Texas Materials Institute, The University of Texas at Austin, Austin, Texas 78712, United States

Delia J. Milliron – McKetta Department of Chemical Engineering and Department of Chemistry, The University of Texas at Austin, Austin, Texas 78712, United States; orcid.org/0000-0002-8737-451X

Brian A. Korgel – McKetta Department of Chemical Engineering, The University of Texas at Austin, Austin, Texas 78712, United States; Texas Materials Institute, The University of Texas at Austin, Austin, Texas 78712, United States; orcid.org/0000-0001-6242-7526

Complete contact information is available at: <https://pubs.acs.org/doi/10.1021/acscatal.2c01001>

Notes

The authors declare no competing financial interest.

■ ACKNOWLEDGMENTS

We gratefully acknowledge the National Science Foundation via grants CHE-1664941 (C.B.M.), CHE-2102307 (C.B.M.), and CHE-1905263 (D.J.M.) as well as the Robert A. Welch Foundation for their generous support through grant nos. F-1436 (C.B.M.), F-1464 (B.A.K.), and F-1848 (D.J.M.). We also acknowledge the Industry/ University Cooperative Research Center (IUCRC) for Next Generation Photovoltaics via grant IIP-1822206 (B.A.K.). Y.J.S. acknowledges the Kwanjeong Educational Foundation Scholarship in South Korea.

■ REFERENCES

- (1) Seitz, L. C.; Dickens, C. F.; Nishio, K.; Hikita, Y.; Montoya, J.; Doyle, A.; Kirk, C.; Vojvodic, A.; Hwang, H. Y.; Nørskov, J. K.; Jaramillo, T. F. A Highly Active and Stable $\text{IrO}_x/\text{SrIrO}_3$ Catalyst for the Oxygen Evolution Reaction. *Science* **2016**, *353*, 1011–1014.
- (2) Laha, S.; Lee, Y.; Podjaski, F.; Weber, D.; Duppel, V.; Schoop, L. M.; Pielnhöfer, F.; Scheurer, C.; Müller, K.; Starke, U.; Reuter, K.; Lotsch, B. V. Ruthenium Oxide Nanosheets for Enhanced Oxygen Evolution Catalysis in Acidic Medium. *Adv. Energy Mater.* **2019**, *9*, 1803795.
- (3) Wygant, B. R.; Kawashima, K.; Mullins, C. B. Catalyst or Precatalyst? The Effect of Oxidation on Transition Metal Carbide, Nitride, and Chalcogenide Oxygen Evolution Catalysts. *ACS Energy Lett.* **2018**, *3*, 2956–2966.
- (4) Dinh, K. N.; Liang, Q.; Du, C.-F.; Zhao, J.; Tok, A. I. Y.; Mao, H.; Yan, Q. Nanostructured Metallic Transition Metal Carbides, Nitrides, Phosphides, and Borides for Energy Storage and Conversion. *Nano Today* **2019**, *25*, 99–121.
- (5) Joo, J.; Kim, T.; Lee, J.; Choi, S.-I.; Lee, K. Morphology-Controlled Metal Sulfides and Phosphides for Electrochemical Water Splitting. *Adv. Mater.* **2019**, *31*, 1806682.
- (6) Masa, J.; Schuhmann, W. The Role of Non-Metallic and Metalloid Elements on the Electrocatalytic Activity of Cobalt and Nickel Catalysts for the Oxygen Evolution Reaction. *ChemCatChem* **2019**, *11*, 5842–5854.
- (7) Jin, S. Are Metal Chalcogenides, Nitrides, and Phosphides Oxygen Evolution Catalysts or Bifunctional Catalysts? *ACS Energy Lett.* **2017**, *2*, 1937–1938.
- (8) Sivanantham, A.; Ganesan, P.; Vinu, A.; Shanmugam, S. Surface Activation and Reconstruction of Non-Oxide-Based Catalysts Through In Situ Electrochemical Tuning for Oxygen Evolution Reactions in Alkaline Media. *ACS Catal.* **2020**, *10*, 463–493.
- (9) McCrory, C. C. L.; Jung, S.; Peters, J. C.; Jaramillo, T. F. Benchmarking Heterogeneous Electrocatalysts for the Oxygen Evolution Reaction. *J. Am. Chem. Soc.* **2013**, *135*, 16977–16987.
- (10) Trotochaud, L.; Ranney, J. K.; Williams, K. N.; Boettcher, S. W. Solution-Cast Metal Oxide Thin Film Electrocatalysts for Oxygen Evolution. *J. Am. Chem. Soc.* **2012**, *134*, 17253–17261.
- (11) Trotochaud, L.; Young, S. L.; Ranney, J. K.; Boettcher, S. W. Nickel–Iron Oxyhydroxide Oxygen-Evolution Electrocatalysts: The Role of Intentional and Incidental Iron Incorporation. *J. Am. Chem. Soc.* **2014**, *136*, 6744–6753.

- (12) Xu, D.; Stevens, M. B.; Cosby, M. R.; Oener, S. Z.; Smith, A. M.; Enman, L. J.; Ayers, K. E.; Capuano, C. B.; Renner, J. N.; Danilovic, N.; Li, Y.; Wang, H.; Zhang, Q.; Boettcher, S. W. Earth-Abundant Oxygen Electrocatalysts for Alkaline Anion-Exchange-Membrane Water Electrolysis: Effects of Catalyst Conductivity and Comparison with Performance in Three-Electrode Cells. *ACS Catal.* **2019**, *9*, 7–15.
- (13) Friebel, D.; Louie, M. W.; Bajdich, M.; Sanwald, K. E.; Cai, Y.; Wise, A. M.; Cheng, M.-J.; Sokaras, D.; Weng, T.-C.; Alonso-Mori, R.; Davis, R. C.; Bargar, J. R.; Nørskov, J. K.; Nilsson, A.; Bell, A. T. Identification of Highly Active Fe Sites in (Ni,Fe)OOH for Electrocatalytic Water Splitting. *J. Am. Chem. Soc.* **2015**, *137*, 1305–1313.
- (14) Klaus, S.; Cai, Y.; Louie, M. W.; Trotochaud, L.; Bell, A. T. Effects of Fe Electrolyte Impurities on Ni(OH)₂/NiOOH Structure and Oxygen Evolution Activity. *J. Phys. Chem. C* **2015**, *119*, 7243–7254.
- (15) Nardi, K. L.; Yang, N.; Dickens, C. F.; Strickler, A. L.; Bent, S. F. Creating Highly Active Atomic Layer Deposited NiO Electrocatalysts for the Oxygen Evolution Reaction. *Adv. Energy Mater.* **2015**, *5*, 1500412.
- (16) Chen, W.; Wang, H.; Li, Y.; Liu, Y.; Sun, J.; Lee, S.; Lee, J.-S.; Cui, Y. In Situ Electrochemical Oxidation Tuning of Transition Metal Disulfides to Oxides for Enhanced Water Oxidation. *ACS Cent. Sci.* **2015**, *1*, 244–251.
- (17) Clament Sagaya Selvam, N.; Kwak, S. J.; Choi, G. H.; Oh, M. J.; Kim, H.; Yoon, W.-S.; Lee, W. B.; Yoo, P. J. Unveiling the Impact of Fe Incorporation on Intrinsic Performance of Reconstructed Water Oxidation Electrocatalyst. *ACS Energy Lett.* **2021**, 4345–4354.
- (18) You, B.; Jiang, N.; Sheng, M.; Bhushan, M. W.; Sun, Y. Hierarchically Porous Urchin-Like Ni₂P Superstructures Supported on Nickel Foam as Efficient Bifunctional Electrocatalysts for Overall Water Splitting. *ACS Catal.* **2016**, *6*, 714–721.
- (19) Im, S. W.; Ahn, H.; Park, E. S.; Nam, K. T.; Lim, S. Y. Electrochemically Activated NiFeO_xH_y for Enhanced Oxygen Evolution. *ACS Appl. Energy Mater.* **2021**, *4*, 595–601.
- (20) Xu, Q.; Jiang, H.; Duan, X.; Jiang, Z.; Hu, Y.; Boettcher, S. W.; Zhang, W.; Guo, S.; Li, C. Fluorination-Enabled Reconstruction of NiFe Electrocatalysts for Efficient Water Oxidation. *Nano Lett.* **2021**, *21*, 492–499.
- (21) Zhang, R.; van Straaten, G.; di Palma, V.; Zafeiropoulos, G.; van de Sanden, M. C. M.; Kessels, W. M. M.; Tsampas, M. N.; Creatore, M. Electrochemical Activation of Atomic Layer-Deposited Cobalt Phosphate Electrocatalysts for Water Oxidation. *ACS Catal.* **2021**, *11*, 2774–2785.
- (22) Kim, J.-H.; Kawashima, K.; Wygant, B. R.; Mabayoje, O.; Liu, Y.; Wang, J. H.; Mullins, C. B. Transformation of a Cobalt Carbide (Co₃C) Oxygen Evolution Precatalyst. *ACS Appl. Energy Mater.* **2018**, *1*, 5145–5150.
- (23) Kawashima, K.; Márquez-Montes, R. A.; Li, H.; Shin, K.; Cao, C. L.; Vo, K. M.; Son, Y. J.; Wygant, B. R.; Chunangad, A.; Youn, D. H.; Henkelman, G.; Ramos-Sánchez, V. H.; Mullins, C. B. Electrochemical Behavior of a Ni₃N OER Precatalyst in Fe-Purified Alkaline Media: The Impact of Self-Oxidation and Fe Incorporation. *Mater. Adv.* **2021**, *2*, 2299–2309.
- (24) Menezes, P. W.; Indra, A.; Das, C.; Walter, C.; Göbel, C.; Gutkin, V.; Schmeißer, D.; Driess, M. Uncovering the Nature of Active Species of Nickel Phosphide Catalysts in High-Performance Electrochemical Overall Water Splitting. *ACS Catal.* **2017**, *7*, 103–109.
- (25) May, K. J.; Carlton, C. E.; Stoerzinger, K. A.; Risch, M.; Suntivich, J.; Lee, Y.-L.; Grimaud, A.; Shao-Horn, Y. Influence of Oxygen Evolution during Water Oxidation on the Surface of Perovskite Oxide Catalysts. *J. Phys. Chem. Lett.* **2012**, *3*, 3264–3270.
- (26) Moureaux, F.; Stevens, P.; Toussaint, G.; Chatenet, M. Timely-Activated 316L Stainless Steel: A Low Cost, Durable and Active Electrode for Oxygen Evolution Reaction in Concentrated Alkaline Environments. *Appl. Catal. B Environ.* **2019**, *258*, No. 117963.
- (27) Schäfer, H.; Sadaf, S.; Walder, L.; Kuepper, K.; Dinklage, S.; Wollschläger, J.; Schneider, L.; Steinhart, M.; Hardege, J.; Daum, D. Stainless Steel Made to Rust: A Robust Water-Splitting Catalyst with Benchmark Characteristics. *Energy Environ. Sci.* **2015**, *8*, 2685–2697.
- (28) Ali Akbari, M. S.; Bagheri, R.; Song, Z.; Najafpour, M. M. Oxygen-Evolution Reaction by Nickel/Nickel Oxide Interface in the Presence of Ferrate(VI). *Sci. Rep.* **2020**, *10*, 8757.
- (29) Kim, S.; Yoo, H. Construction of a Pliable Electrode System for Effective Electrochemical Oxygen Evolution Reaction: Direct Growth of Nickel/Iron/Selenide Nanohybrids on Nickel Foil. *ACS Sustainable Chem. Eng.* **2020**, *8*, 13859–13867.
- (30) Hu, X.; Tian, X.; Lin, Y.-W.; Wang, Z. Nickel Foam and Stainless Steel Mesh as Electrocatalysts for Hydrogen Evolution Reaction, Oxygen Evolution Reaction and Overall Water Splitting in Alkaline Media. *RSC Adv.* **2019**, *9*, 31563–31571.
- (31) Suen, N.-T.; Hung, S.-F.; Quan, Q.; Zhang, N.; Xu, Y.-J.; Chen, H. M. Electrocatalysis for the Oxygen Evolution Reaction: Recent Development and Future Perspectives. *Chem. Soc. Rev.* **2017**, *46*, 337–365.
- (32) Chen, G.; Zhou, W.; Guan, D.; Sunarso, J.; Zhu, Y.; Hu, X.; Zhang, W.; Shao, Z. Two Orders of Magnitude Enhancement in Oxygen Evolution Reactivity on Amorphous Ba_{0.5}Sr_{0.5}Co_{0.8}Fe_{0.2}O_{3-δ} Nanofilms with Tunable Oxidation State. *Sci. Adv.* **2017**, *3*, No. e1603206.
- (33) Son, Y. J.; Kawashima, K.; Wygant, B. R.; Lam, C. H.; Burrow, J. N.; Celio, H.; Dolocan, A.; Ekerdt, J. G.; Mullins, C. B. Anodized Nickel Foam for Oxygen Evolution Reaction in Fe-Free and Unpurified Alkaline Electrolytes at High Current Densities. *ACS Nano* **2021**, *15*, 3468–3480.
- (34) Alsabet, M.; Grden, M.; Jerkiewicz, G. Electrochemical Growth of Surface Oxides on Nickel. Part 1: Formation of α-Ni(OH)₂ in Relation to the Polarization Potential, Polarization Time, and Temperature. *Electrocatalysis* **2011**, *2*, 317–330.
- (35) Alsabet, M.; Grden, M.; Jerkiewicz, G. Electrochemical Growth of Surface Oxides on Nickel. Part 2: Formation of β-Ni(OH)₂ and NiO in Relation to the Polarization Potential, Polarization Time, and Temperature. *Electrocatalysis* **2014**, *5*, 136–147.
- (36) Alsabet, M.; Grden, M.; Jerkiewicz, G. Electrochemical Growth of Surface Oxides on Nickel. Part 3: Formation of β-NiOOH in Relation to the Polarization Potential, Polarization Time, and Temperature. *Electrocatalysis* **2015**, *6*, 60–71.
- (37) Oshchepkov, A. G.; Bonnefont, A.; Savinova, E. R. On the Influence of the Extent of Oxidation on the Kinetics of the Hydrogen Electrode Reactions on Polycrystalline Nickel. *Electrocatalysis* **2020**, *11*, 133–142.
- (38) Lyons, M. E. G.; Doyle, R. L.; Godwin, I.; O'Brien, M.; Russell, L. Hydrous Nickel Oxide: Redox Switching and the Oxygen Evolution Reaction in Aqueous Alkaline Solution. *J. Electrochem. Soc.* **2012**, *159*, H932–H944.
- (39) Doyle, R. L.; Godwin, I. J.; Brandon, M. P.; Lyons, M. E. G. Redox and Electrochemical Water Splitting Catalytic Properties of Hydrated Metal Oxide Modified Electrodes. *Phys. Chem. Chem. Phys.* **2013**, *15*, 13737–13783.
- (40) Rebouillat, S.; Lyons, M. E. G.; Brandon, M. P.; Doyle, R. L. Paving the Way to The Integration of Smart Nanostructures: Part II: Nanostructured Microdispersed Hydrated Metal Oxides for Electrochemical Energy Conversion and Storage Applications. *Int. J. Electrochem. Sci.* **2011**, *6*, 5830–5917.
- (41) Batchelor, A. S.; Boettcher, S. W. Pulse-Electrodeposited Ni-Fe (Oxy)Hydroxide Oxygen Evolution Electrocatalysts with High Geometric and Intrinsic Activities at Large Mass Loadings. *ACS Catal.* **2015**, *5*, 6680–6689.
- (42) Wang, M.; Wei, Y.-S.; Zou, L.; Wang, H.-F.; Shen, S.; Xu, Q. Revealing Active Function of Multicomponent Electrocatalysts from In Situ Nickel Redox for Oxygen Evolution. *J. Phys. Chem. C* **2021**, *125*, 16420–16427.
- (43) Seh, Z. W.; Kibsgaard, J.; Dickens, C. F.; Chorkendorff, I.; Nørskov, J. K.; Jaramillo, T. F. Combining Theory and Experiment in

Electrocatalysis: Insights into Materials Design. *Science* **2017**, *355*, No. eaad4998.

(44) Morales-Guio, C. G.; Liardet, L.; Hu, X. Oxidatively Electrodeposited Thin-Film Transition Metal (Oxy)Hydroxides as Oxygen Evolution Catalysts. *J. Am. Chem. Soc.* **2016**, *138*, 8946–8957.

(45) Roy, C.; Sebok, B.; Scott, S. B.; Fiordaliso, E. M.; Sørensen, J. E.; Bodin, A.; Trimarco, D. B.; Damsgaard, C. D.; Vesborg, P. C. K.; Hansen, O.; Stephens, I. E. L.; Kibsgaard, J.; Chorkendorff, I. Impact of Nanoparticle Size and Lattice Oxygen on Water Oxidation on NiFeOxHy. *Nat. Catal.* **2018**, *1*, 820–829.

(46) Dionigi, F.; Zhu, J.; Zeng, Z.; Merzdorf, T.; Sarodnik, H.; Gliech, M.; Pan, L.; Li, W.-X.; Greeley, J.; Strasser, P. Intrinsic Electrocatalytic Activity for Oxygen Evolution of Crystalline 3d-Transition Metal Layered Double Hydroxides. *Angew. Chem., Int. Ed.* **2021**, *60*, 14446–14457.

(47) Corrigan, D. A.; Bendert, R. M. Effect of Coprecipitated Metal Ions on the Electrochemistry of Nickel Hydroxide Thin Films: Cyclic Voltammetry in 1M KOH. *J. Electrochem. Soc.* **1989**, *136*, 723.

(48) Dionigi, F.; Zeng, Z.; Sinev, I.; Merzdorf, T.; Deshpande, S.; Lopez, M. B.; Kunze, S.; Zegkinoglou, I.; Sarodnik, H.; Fan, D.; Bergmann, A.; Drnec, J.; de Araujo, J. F.; Gliech, M.; Teschner, D.; Zhu, J.; Li, W.-X.; Greeley, J.; Cuenya, B. R.; Strasser, P. In-Situ Structure and Catalytic Mechanism of NiFe and CoFe Layered Double Hydroxides during Oxygen Evolution. *Nat. Commun.* **2020**, *11*, 2522.

(49) McKeown, D. A.; Hagans, P. L.; Cayette, L. P. L.; Russell, A. E.; Swider, K. E.; Rolison, D. R. Structure of Hydrated Ruthenium Oxides: Implications for Charge Storage. *J. Phys. Chem. B* **1999**, *103*, 4825–4832.

(50) Bode, H.; Dehmelt, K.; Witte, J. Zur Kenntnis Der Nickelhydroxidelektrode—I. Über Das Nickel (II)-Hydroxidhydrat. *Electrochim. Acta* **1966**, *11*, 1079–1087.

(51) Van der Ven, A.; Morgan, D.; Meng, Y. S.; Ceder, G. Phase Stability of Nickel Hydroxides and Oxyhydroxides. *J. Electrochem. Soc.* **2006**, *153*, A210–A215.

(52) Lyons, M. E. G.; Cakara, A.; O'Brien, P.; Godwin, I.; Doyle, R. L. Redox, PH Sensing and Electrolytic Water Splitting Properties of Electrochemically Generated Nickel Hydroxide Thin Films in Aqueous Alkaline Solution. *Int. J. Electrochem. Sci.* **2012**, *7*, 11768–11795.

(53) Lyons, M. E. G.; Russell, L.; O'Brien, M.; Doyle, R. L.; Godwin, I.; Brandon, M. P. Redox Switching and Oxygen Evolution at Hydrated Oxyhydroxide Modified Nickel Electrodes in Aqueous Alkaline Solution: Effect of Hydrated Oxide Thickness and Base Concentration. *Int. J. Electrochem. Sci.* **2012**, *7*, 2710–2763.

(54) Fleischmann, S.; Mitchell, J. B.; Wang, R.; Zhan, C.; Jiang, D.; Presser, V.; Augustyn, V. Pseudocapacitance: From Fundamental Understanding to High Power Energy Storage Materials. *Chem. Rev.* **2020**, *120*, 6738–6782.

(55) Bediako, D. K.; Costentin, C.; Jones, E. C.; Nocera, D. G.; Savéant, J.-M. Proton–Electron Transport and Transfer in Electrocatalytic Films. Application to a Cobalt-Based O₂-Evolution Catalyst. *J. Am. Chem. Soc.* **2013**, *135*, 10492–10502.

(56) Zheng, J.; Yan, Y.; Xu, B. Correcting the Hydrogen Diffusion Limitation in Rotating Disk Electrode Measurements of Hydrogen Evolution Reaction Kinetics. *J. Electrochem. Soc.* **2015**, *162*, F1470–F1481.

(57) Stevens, M. B.; Trang, C. D. M.; Enman, L. J.; Deng, J.; Boettcher, S. W. Reactive Fe-Sites in Ni/Fe (Oxy)Hydroxide Are Responsible for Exceptional Oxygen Electrocatalysis Activity. *J. Am. Chem. Soc.* **2017**, *139*, 11361–11364.

(58) Görlin, M.; Cherev, P.; Ferreira de Araujo, J.; Reier, T.; Dresp, S.; Paul, B.; Krähnert, R.; Dau, H.; Strasser, P. Oxygen Evolution Reaction Dynamics, Faradaic Charge Efficiency, and the Active Metal Redox States of Ni–Fe Oxide Water Splitting Electrocatalysts. *J. Am. Chem. Soc.* **2016**, *138*, 5603–5614.

(59) Farhat, R.; Dhainy, J.; Halaoui, L. I. OER Catalysis at Activated and Codeposited NiFe-Oxo/Hydroxide Thin Films Is Due to

Postdeposition Surface-Fe and Is Not Sustainable without Fe in Solution. *ACS Catal.* **2020**, *10*, 20–35.

(60) Zhang, T.; Nellist, M. R.; Enman, L. J.; Xiang, J.; Boettcher, S. W. Modes of Fe Incorporation in Co–Fe (Oxy)Hydroxide Oxygen Evolution Electrocatalysts. *ChemSusChem* **2019**, *12*, 2015–2021.

(61) Kuai, C.; Xu, Z.; Xi, C.; Hu, A.; Yang, Z.; Zhang, Y.; Sun, C.-J.; Li, L.; Sokaras, D.; Dong, C.; Qiao, S.-Z.; Du, X.-W.; Lin, F. Phase Segregation Reversibility in Mixed-Metal Hydroxide Water Oxidation Catalysts. *Nat. Catal.* **2020**, *3*, 743–753.

(62) Kuai, C.; Xi, C.; Hu, A.; Zhang, Y.; Xu, Z.; Nordlund, D.; Sun, C.-J.; Cadigan, C. A.; Richards, R. M.; Li, L.; Dong, C.-K.; Du, X.-W.; Lin, F. Revealing the Dynamics and Roles of Iron Incorporation in Nickel Hydroxide Water Oxidation Catalysts. *J. Am. Chem. Soc.* **2021**, *143*, 18519–18526.

(63) Terezo, A. J.; Bisquert, J.; Pereira, E. C.; Garcia-Belmonte, G. Separation of Transport, Charge Storage and Reaction Processes of Porous Electrocatalytic IrO₂ and IrO₂/Nb₂O₅ Electrodes. *J. Electroanal. Chem.* **2001**, *508*, 59–69.

(64) Bisquert, J. Theory of the Impedance of Electron Diffusion and Recombination in a Thin Layer. *J. Phys. Chem. B* **2002**, *106*, 325–333.

(65) Vrabel, H.; Moehl, T.; Grätzel, M.; Hu, X. Revealing and Accelerating Slow Electron Transport in Amorphous Molybdenum Sulphide Particles for Hydrogen Evolution Reaction. *Chem. Commun.* **2013**, *49*, 8985–8987.

(66) Chuminjak, Y.; Daothong, S.; Reanpang, P.; Mensing, J. P.; Phokharatkul, D.; Jakmunee, J.; Wisitsoraat, A.; Tuantranont, A.; Singjai, P. Electrochemical Energy-Storage Performances of Nickel Oxide Films Prepared by a Sparking Method. *RSC Adv.* **2015**, *5*, 67795–67802.

(67) Dette, C.; Hurst, M. R.; Deng, J.; Nellist, M. R.; Boettcher, S. W. Structural Evolution of Metal (Oxy)Hydroxide Nanosheets during the Oxygen Evolution Reaction. *ACS Appl. Mater. Interfaces* **2019**, *11*, 5590–5594.

Recommended by ACS

Deciphering the *In Situ* Surface Reconstruction of Supercapacitive Bimetallic Ni-Co Oxyphosphide during Electrochemical Activation Using Multivariate Statistical...

Amina A. Saleh, Nageh K. Allam, *et al.*

JUNE 06, 2022

ACS APPLIED ENERGY MATERIALS

READ 

Substitutional Doping Engineering toward W₂N Nanorod for Hydrogen Evolution Reaction at High Current Density

Zixuan Dan, Hui Meng, *et al.*

JUNE 14, 2022

ACS MATERIALS LETTERS

READ 

Nickel Site Modification by High-Valence Doping: Effect of Tantalum Impurities on the Alkaline Water Electro-Oxidation by NiO Probed by Operando Raman Spectroscopy

Nicole A. Sagui, İlknur Bayrak Pehlivan, *et al.*

MAY 17, 2022

ACS CATALYSIS

READ 

In Situ-Activated Indium Nanoelectrocatalysts for Highly Active and Selective CO₂ Electroreduction around the Thermodynamic Potential

Lushan Ma, Qiang Li, *et al.*

JULY 05, 2022

ACS CATALYSIS

READ 

Get More Suggestions >